INTERPLAY BETWEEN QUANTUM SIZE EFFECT AND STRAIN EFFECT ON GROWTH OF NANOSCALE METAL THIN FILM

by

Miao Liu

A dissertation submitted to the faculty of
The University of Utah
in partial fulfillment of the requirements for the degree of

Doctor of Philosophy

Department of Materials Science and Engineering

The University of Utah

December 2012

The University of Utah Graduate School

STATEMENT OF DISSERTATION APPROVAL

The dissertation of **Miao Liu**

has been approved by the following supervisory committee members:

Feng Liu	, Chair	**10/22/2012** Date Approved
Gerald B. Stringfellow	, Member	**10/22/2012** Date Approved
Michael A. Scarpulla	, Member	**10/23/2012** Date Approved
Ashutosh Tiwari	, Member	Date Approved
Yong-Shi Wu	, Member	Date Approved

and by **Feng Liu**, Chair of the Department of **Materials Science and Engineering**

and by Charles A. Wight, Dean of The Graduate School.

ABSTRACT

The focus of this dissertation is to explore novel effects in metal nanofilms, particularly, the quantum size effect (QSE) and strain effect, through the methodology of first-principles density functional theory (DFT) calculations. The QSE has already been shown to affect many properties of metal nanofilms, such as surface energy, work function, and even superconducting transition temperature. Based on the extensive DFT calculations that I carried out in the last five years, we further demonstrate that several new properties of metal nanofilms, including edge/surface stress, elastic constants, and adatom-adatom binding energy can also be modulated by QSE to exhibit strong thickness dependence. Specifically, this dissertation includes the following five chapters of topics: (1) interplay between strain effect and quantum size effect in metal nanofilm; (2) quantum manifestation of elastic constants in nanostructures; (3) QSE on adatom-adatom binding energy and island nucleation; (4) quantum manifestations of graphene edge stress and edge instability; (5) bistability of nanoscale islands induced by anisotropic stress. Overall, my dissertation research not only has explained a number of puzzling experimental observations and resolved some existing controversies, but also made some interesting theoretical predictions in novel quantum aspects of thin film growth and nanomechanics. It is my hope that these studies will further our fundamental understanding of QSE and strain effect in metal nanofilms, with broader implications in other low-dimensional nanostructures as well as in potential technological applications of nanostructures.

CONTENTS

LIST OF FIGURES

CHAPTER 1

INTRODUCTION TO QUANTUM SIZE EFFECT

1.1 Introduction

The scientific theme of this dissertation is to study quantum size effect (QSE) in metal nanofilms epitaxially grown on a substrate. QSE is generally referred to as an effect induced by quantum confinement of electrons in low-dimensional nanostructures. As the size of nanostructures is reduced to nanometer scale comparable to the electron Fermi wavelength, the translational motion of electrons, which has a characteristic length scale of Fermi wavelength, is confined, giving rise to new discrete electronic states (quantum confinement states) that change the energy landscape of electrons. Consequently, QSE is one major effect, in addition to surface effect, that makes the properties of nanostructures distinctively different from those of their bulk counterpart. Apparently, QSE exhibits a strong size and shape dependence, because the size and shape of the nanostructure will alter the strength and form of the quantum confinement. The size and shape dependence not only makes the fundamental study of QSE scientifically interesting but also technologically appealing, providing a unique opportunity to tailor the properties and functionalities of nanostructures, especially those aroused from QSE, by tuning their size and shape for potential applications. This is one of the important scientific foundations for modern nanotechnology. Therefore, studying the physical mechanisms underlying the size dependence of QSE in various nanostructures is of critical importance. Specifically, the focus of the present dissertation is to investigate QSE and its impact on physical properties of metal nanofilms, including surface energy, surface stress, surface adsorption, adatom-adatom binding energy, elastic constant, and their implications

on growth stability and morphology of epitaxial metal nanofilms.

1.2 Quantum Size Effect

Generally, QSE is much more pronounced in metal nanostructures than in semiconductor and insulator nanostructures. This is because the electron Fermi wavelength of most metals (in the range of 3-5Å) [1] is shorter than that in semiconductors and insulators. The history of studying QSE in metal nanofilms goes back almost half a century. The earliest work of QSE was by Jackeic *et al.*, who experimentally observed an electron standing wave in Pb film in 1971 [2]. Later, in 1976, Schutler performed a comprehensive theoretical study to show that electron charge density, potential energy, and work function in freestanding metal thin films all display a strong dependence on the film thickness induced by QSE, using self-consistent jellium model calculations [3]. In 1983, Feibelman *et al.* confirmed the work function oscillation in metal film and found that surface energy also oscillates as a function of film thickness using the same calculation method as Schutler [4]. Shortly after, several experiments confirmed the above theoretical predictions. For example, Marliere measured the work function of indium film and found its work function to vary with the film thickness [5], and Jalochowski *et al.* showed oscillation of electrical resistivity of thin Pb(111) film as a function of film thickness [6]. Taking advantage of the rapid development of first-principles calculation methods and thin film growth techniques, especially molecular beam epitaxy (MBE), the study of QSE has expanded and advanced significantly in the last decade. Experimentally, many physical properties, including thermal stability [7-9], work function [10,11], superconductivity [12,13], and surface-mediated chemical reaction [14], have been measured for various metal thin films. For example, Czoschke *et al.* demonstrated that the film stability of Pb(111) film displays an odd-even oscillation as a function of thickness [7], as shown in Fig. 1.1(a); Guo *et al.* demonstrated that the superconducting transition temperature (Tc) of Pb(111) thin film exhibits a surprising thickness dependence [12], as shown in Fig. 1.1(b). Theoretically, beyond the original work by Schulter [3], Zhang *et al.* proposed an "electronic growth model" underlying the QSE on growth of metal films [15]. Mei and Chou carried out first-principles density functional theory (DFT)

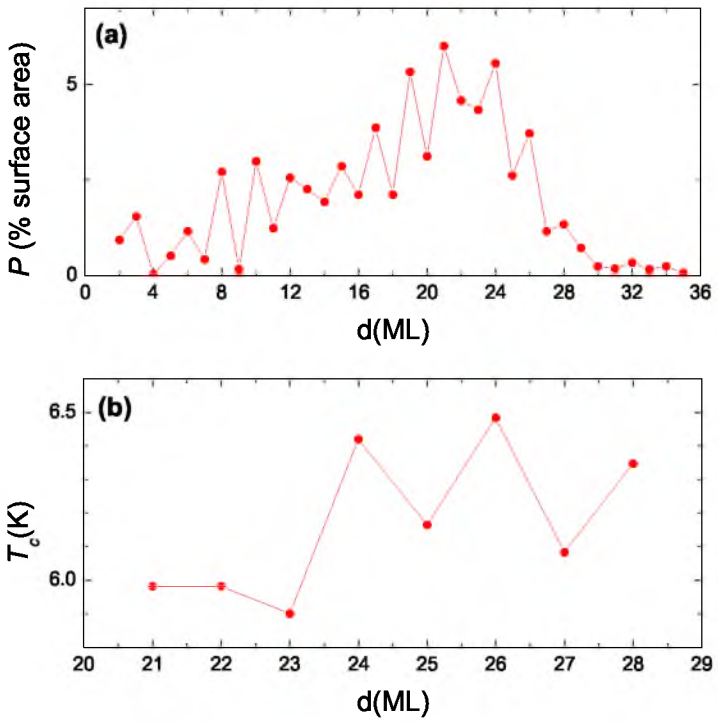

Figure 1.1. Experimental demonstrations of QSE in Pb(111) film: (a) film stability oscillating as a function of film thickness [7]; (b) superconducting transition temperature verses film thickness [12].

calculations of QW states, surface energy, and work function of Pb(111) film as a function of thickness [16]. In addition to thermodynamic properties, first-principles calculations by Chan *et al.* [17] and Ma *et al.* [18] also showed that QSE can affect surface growth kinetic parameters, such as surface diffusion barrier, which provided critical information for explaining the experimental results that indicated the role of QSE played in affecting the growth morphology of metal thin films [19, 20].

Fundamentally, most salient features of QSE in metal films can be captured by the free electron gas model, as reviewed below. The electrons in a solid behave like free electrons except for a different effective mass, having the following general energy-momentum dispersion relation:

$$E = \frac{\hbar^2}{2m}(k_x^2 + k_y^2 + k_z^2) \tag{1.1}$$

where E is the kinetic energy of the electron, m is the free electron mass, $\hbar$ denotes Plancks's constant, and k_x, k_y, and k_z are the wave vector in x, y, and z direction, respectively. Eq. 1.1 also illustrates the spherical shape of occupied states below the Fermi surface in momentum space. For a metal thin film of thickness d, the electrons are confined in the surface normal direction (z-direction) by the surface (solid-vacuum interface) and film/substrate interface, forming the quantum well (QW) states according to the Sommerfeld-Bohr quantization condition:

$$2k_{(z,n)}d + 2\Phi = 2\pi n \tag{1.2}$$

where $k_{(z,n)}$ is the allowed wave vector component in z-direction, n takes integer values, and Φ accounts for the phase shift at the film boundaries. Consequently, the electron dispersion relation of QW states becomes

$$E = \frac{\hbar^2}{2m}(k_x^2 + k_y^2) + E_{(z,n)} \tag{1.3}$$

where $E_{(z,n)}$ is the discrete eigen-energy determined by the Sommerfeld-Bohr quantization condition. Thus, a set of discrete subbands form, as shown in Fig. 1.2.

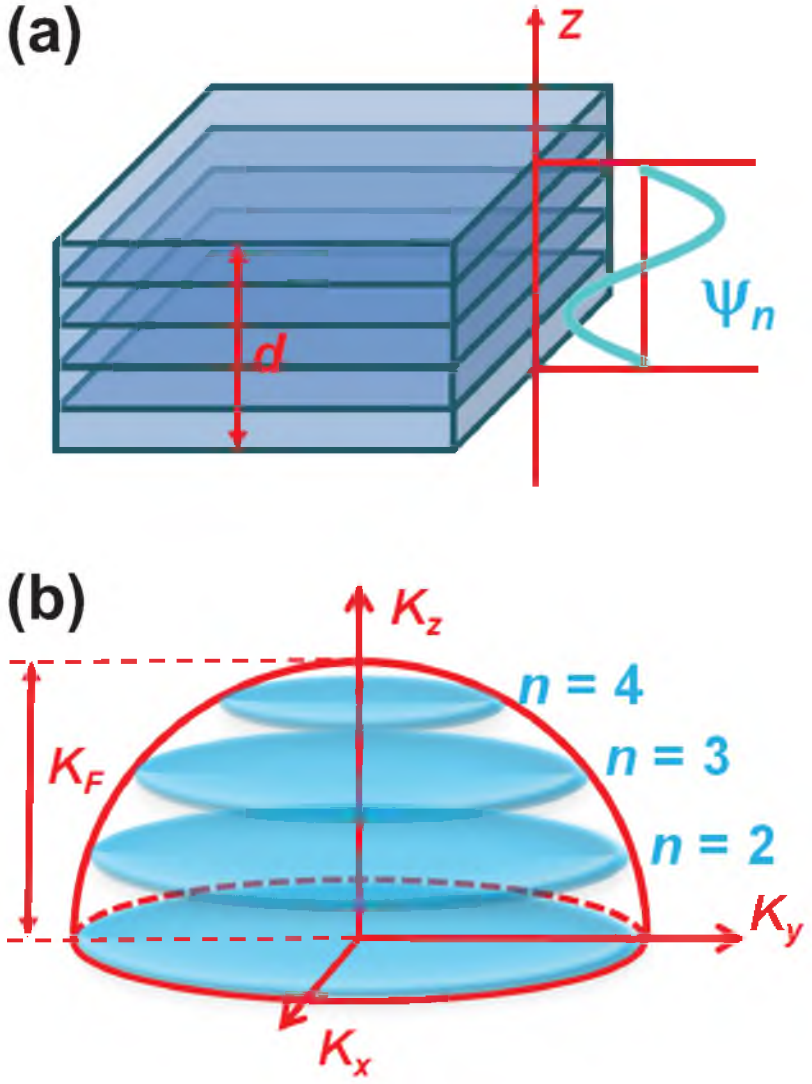

Figure 1.2. Physical origin of QSE in thin film. (a) Electron confinement in thin film. (b)Occupied states in metal thin film.

The Fermi level of the film (E_f) can be derived as [21, 22, 23]:

$$E_f(d) = \frac{2dk_F}{3N\pi}E_f + \langle E_{(z,n)}\rangle \tag{1.4}$$

where $\langle E_(z,n)\rangle$ averages over all the bands below the highest occupied subbands. E_F and k_F are the Fermi energy and Fermi wave number of the bulk metal, respectively. Plotting the eigen values of QW states (Eq. 1.3) and Fermi wavelength (λ_F) (Eq. 1.4) together in Fig. 1.3(a), it is clear that the energies of QW states decrease with the increasing film thickness. Also, as the film thickness increases, the Fermi energy exhibits a cusp whenever an empty subband crosses the Fermi level to become an occupied band. Consequently, the thin film Fermi energy oscillates as a function of film thickness and eventually converges to the bulk Fermi energy at very large film thickness. The cusps are separated by a thickness of $\lambda_F/2$, which means that at the Fermi level, the general quantization condition becomes $d = \lambda_F/2$. Because of the $\lambda_F/2$ oscillations of the Fermi level, the charge density of the slab oscillates as well. Consequently, the total energy of the film can be derived as [21, 22]:

$$E_t(d) = \frac{ms}{2\pi\hbar^2}\sum_{n\leq N}(E_F^2 - E_{z,n}^2) \tag{1.5}$$

and the surface energy E_s is

$$E_s(d) = \frac{ms}{2\pi\hbar^2}(\sum_{n\leq N}\frac{E_F^2 - E_{z,n}^2}{E_F^2} - \frac{4}{5}\frac{dk_F}{\pi}) \tag{1.6}$$

Figure 1.3(b) and 1.3(c) show the work function and surface energy plot as a function of film thickness, based on the analytical solution of the free electron gas model (Eq. 1.4 and 1.6), respectively. There are the cusp-shape oscillations in Fermi energy with a period of $\lambda_F 2$, and the oscillation amplitude decreases with the increasing film thickness. When we only take the integer values of film thickness, both work function and surface energy display an odd-even oscillation, as shown in Fig 1.3(b) and (c).

From the quantization condition (Eq. 1.2) and Fig. 1.3, we can see that the oscillatory behavior in the film properties induced by quantum confinement are determined

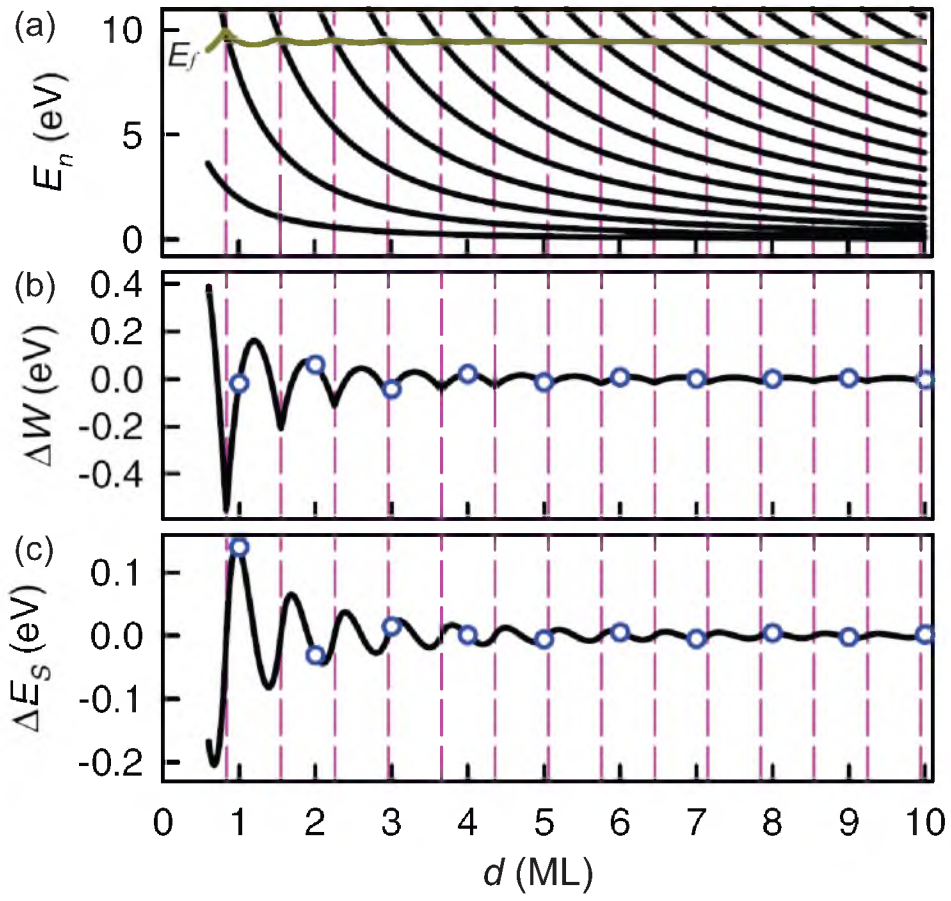

Figure 1.3. Results from free electron gas model. From top to bottom: (a)The quantized electronic QW states and Fermi level; (b)workfunction; (c) surface energy. Subband crossings are marked by vertical dashed lines. The value of workfunction and surface energy at integer d are marked by circles.

by both film atomic interlayer spacing (d_0) and the Fermi wavelength ($\lambda_F/2$). If $\lambda_F/2 : d_0 = 1$, the thickness of film matches the cusp period; thus, the value of Fermi level, work function, and surface energy are the values of cusp nodal points. Consequently, the oscillation magnitude of surface energy and work function become very small, corresponding to weak QSE. Especially for Pb(111) films, which has been widely used as a model system for studying QSE, $\lambda_F/2 : d_0 = 1 : 1.44 \approx 2 : 3$, which gives two striking QSE features: (1) Pb(111) film displays strong odd-even oscillation, because of the matching relation between d_0 and $\lambda_F/2$; (2) the oscillation is modulated by a beating pattern with a period of 9 MLs, due to the imperfect matching between d_0 and $\lambda_F/2$.

1.3 Summary

The remaining chapters of this dissertation are arranged as follows. In Chapter 2, I will present my study of "the interplay between quantum size effect and strain effect on growth of nanoscale metal thin film." We develop a theoretical framework to investigate the interplay between the quantum size effect and strain effect on the stability of metal nanofilms. The quantum size effect and strain effect are shown to be coupled through the concept of "quantum electronic stress". First-principles calculations reveal large quantum oscillations in the surface stress of metal nanofilms as a function of film thickness, which adds extrinsically additional strain-coupled quantum oscillations to the surface energy of strained metal nanofilms. Our theory enables a quantitative estimation of the amount of strain in experimental samples, and suggests strain to be an important factor contributing to the discrepancies between the existing theories and experiments.

In Chapter 3, I will focus on the topic of "quantum manifestation of elastic constants in nanostructures." Generally, there are two distinct effects in modifying the properties of low-dimensional nanostructures: surface effect due to increased surface-volume ratio and quantum size effect due to quantum confinement in reduced dimensions. The surface effect has been widely shown to affect the elastic constants and mechanical properties of nanostructures. Here, using Pb nanofilm and graphene nanoribbon as model systems, we demonstrate the quantum size effect

on the elastic constants of nanostructures by first-principles calculations. We show that generally, quantum size effect is dominant in affecting the elastic constants of metallic nanostructures while surface effect is more pronounced in semiconductor and insulator nanostructures. Our findings have broad implications in quantum aspects of nanomechanics.

In Chapter 4, the topic of "thickness-dependent adatom-adatom binding energy on Pb(111): quantum size effect on island nucleation" will be addressed. Quantum size effect is well known to alter the intrinsic properties of nanostructures as well as the interactions between an adatom and the surface of nanostructures. Here, using first-principles calculations, we demonstrate QSE to alter the interaction between adatoms on the surface of nanostructures. A thickness-dependent oscillation is found in the adatom-adatom binding energies on Pb(111). We discuss these results in relation to the thickness-dependent island nucleation density as observed from recent experiments. We show that island density is not just modulated by the QSE-induced changing adatom diffusion barrier, as commonly perceived before, but also by the adatom-adatom binding energy, especially for small critical island size at low growth temperature.

In Chapter 5, I will present our work on "quantum manifestations of graphene edge stress and edge instability." We have performed first-principles calculations of graphene edge stresses, which display two interesting quantum manifestations absent from the classical interpretation: the armchair edge stress oscillates with a nanoribbon width, and the zigzag edge stress is noticeably reduced by spin polarization. Such quantum stress effects in turn manifest in mechanical edge twisting and warping instability, showing features not captured by empirical potentials or continuum theory. Edge adsorption of H and Stone-Wales reconstruction are shown to provide alternative mechanisms in relieving the edge compression and hence, to stabilize the planar edge structure.

Chapter 6 does not involve any QSE, but still focuses on the stress state occurring along the interface. In that part, we will show the "bistability of nanoscale Ag islands on a Si(111)-(4×1)-In surface induced by anisotropic stress." Experimentally, our collaborator demonstrates the existence of two stability regimes of Ag nanoislands

grown on a Si(111)-(4×1)-In surface: a conventional regime at low temperature where only one island shape is stable, and an unconventional regime at room temperature (RT) where isotropic compact islands coexist with anisotropic elongated ones. Using first-principles calculations, we show that the unusual bistability at RT arises from the fact that the Ag nanoislands are under anisotropic stress, supporting a recent theoretical prediction by Zandvliet and van Gastel [24].

1.4 Reference

[1] N. W. Ashcroft and N. D. Mermin, Solid State Physics (Thomson Learning, New York, 1976).

[2] R. C. Jaklevic, J. Lambe, M. Mikkor, and W. C. Vassell, Phys. Rev. Lett. **26**, 88 (1971).

[3] F. K. Schulte, Surf. Sci. **55**, 428 (1976).

[4] P. J. Feibelman, Phys. Rev. B **27**, 1991 (1983).

[5] C. Marliere, Vacuum **41**, 1192 (1990).

[6] M. Jalochowski and E. Bauer, Phys. Rev. B **38**, 5272 (1988).

[7] P. Czoschke, H. Hong, L. Basile, and T.C. Chiang. Phys. Rev. Lett. **93**, 036103 (2004).

[8] M.H. Upton, C.M. Wei, M.Y. Chou, T. Miller, T.C. Chiang, Phys. Rev. Lett. **93**,026802 (2004).

[9] M.M. Ozer, Y. Jia, B. Wu, Z.Y. Zhang, H.H. Weitering, Phys. Rev. B **72**, 113409 (2005).

[10] Y. Qi, X. Ma, P. Jiang, S. H. Ji, Y. S. Fu, J.-F. Jia, Q.-K. Xue, S. B. Zhang, Appl. Phys. Lett. **90**, 013109 (2007).

[11] J. Kim, S. Qin, W. Yao, Q. Niu, M. Y. Chou, and C.-K. Shih, PNAS **107**, 12761 (2010).

[12] Y. Guo, Y. F. Zhang, X. Y. Bao, T. Z. Han, Z. Tang, L. X. Zhang, W. G. Zhu, E. G. Wang, Q. Niu, Z. Q. Qiu, J.-F. Jia, Z. X. Zhao, Q.-K. Xue, Science **306**, 1915 (2004).

[13] M. Ozer, Y. Jia, Z.Y. Zhang, J. R. Thompson, and H. H. Weitering, Science **316**, 1594 (2007).

[14] X. Ma, P. Jiang, Y. Qi, J.-F. Jia, Y. Yang, W. Duan, W.-X. Li, X. Bao, S. B. Zhang, and Q.-K. Xue, PNAS **104**, 9204 (2007).

[15] Z. Zhang, Q. Niu, C.-K. Shih, Phys. Rev. lett. **80**, 5381 (1998).

[16] C.M. Wei and M.Y. Chou, Phys. Rev. B, **66**, 233408 (2002).

[17] T.-L.Chan, C. Z. Wang, M. Hupalo, M. C. Tringides, and K. M. Ho, Phys. Rev. Lett. **96**, 226102 (2006).

[18] L.-Y. Ma, L. Tang, Z.-L. Guan, K. He, K. An, X.-C. Ma, J.-F. Jia, Q.-K. Xue, Y. Han, S. Huang, and F. Liu, Phys. Rev. Lett. **97**, 266102 (2006).

[19] S. M. Binz, M. Hupalo, and M. C. Tringides, Phys. Rev. B **78**, 193407 (2008).

[20] S. M. Binz, M. Hupalo, and M. C. Tringides, J. Appl. Phys. **105**, 094307 (2009).

[21] B. Wu and Z. Zhang, Phys. Rev. B, **77**, 035410 (2008).

[22] Y. Han and D.-J. Liu, Phys. Rev. B, **80**, 155404 (2009).

[23] T. Miller, M. Y. Chou, and T.-C. Chiang, Phys. Rev. Lett. **102**, 236803 (2009).

[24] H. J. W. Zandvliet and R. van Gastel, Phys. Rev. Lett. **99**, 136103 (2007).

CHAPTER 2

INTERPLAY BETWEEN QUANTUM SIZE EFFECT AND STRAIN EFFECT ON GROWTH OF NANOSCALE METAL THIN FILM

2.1 Introduction

When the thickness of a metal film is reduced to the range of the electron Fermi wavelength, quantum confinement becomes prominent for forming discrete quantum well states, giving rise to various manifestations of quantum size effect (QSE) [1]. In particular, the QSE has been shown to be a dominant factor in the growth of metal nanofilms on semiconductor substrates [1-5] in the so-called electronic growth regime [2]. On the other hand, the strain effect is ubiquitous in heteroepitaxial growth of semiconductor and metal thin films [6, 7]. A few recent studies [8-12] have considered both effects on metal thin film growth. One thermodynamic theory [8] studied both effects on film stability, and two kinetic models [10, 11] assumed growth parameters to be dependent of island height and radius due to the QSE and strain effects. However, majority studies have focused on one effect while neglecting the other, and those few studies which considered both effects have been generally limited to treat them as two independent additive effects. This is mostly because fundamentally, no theory is available to assess how the QSE may change the stress state of the film, and conversely, how strain may alter the QSE. Therefore, it is very important to establish a theoretical framework that underlies the QSE on surface stress that in turn underlies the interplay between the QSE and strain effect.

The Pb(111) film grown on Si(111) substrate has been extensively studied as a model system for QSE [3-5, 13, 14]. The almost perfect matching between the Pb

Fermi wavelength and its interlayer spacing in the (111) direction gives rise to two striking QSE features in Pb film: the odd-even oscillations and beating patterns exhibited in many properties such as surface energy and stability. These two main features have been agreed upon by all theoretical and experimental studies [3-5, 13, 14]. However, there remain some outstanding discrepancies. Oscillation patterns may vary slightly from one experimental sample to another [13-16]. First-principles calculations [4] predicted that the odd-even oscillations in surface energy essentially die out at a thickness of ∼20 monolayers (MLs), while experiments, in contrast, have seen the large oscillations sustain even beyond 30 MLs [13, 14]. One origin of the discrepancies was attributed to Pb/Si interface that causes a phase shift in the oscillation patterns[3], but the strain effect has been mostly overlooked so far.

Because of the large lattice mismatch, the Pb (111)film tends to grow on Si(111) substrate by adopting a 10-to-9 epi relation to minimize interfacial misfit strain [17, 18]. Even so, Pb film can still experience up to ±3% strain depending on the film orientation relative to Si surface [17]. The measurement of interlayer spacing by X-ray diffraction [13] suggested that the strain in Pb film be small based on bulk Poisson ratio, but the actual amount of in-plane strain remains uncertain, because the ultrathin film may not follow the bulk Poisson ratio, especially in the presence of QSE that modifies the interlayer spacing. Overall, the strain effect has not been studied adequately in relation with the QSE, because of the lack of theory underlying their relationship and because the direct measurement of strain in the film is very difficult.

2.2 Methodology

In this chapter, we develop a general theory underlying the fundamental relationship between the QSE and strain effect in the formulation of surface energy through the concept of "quantum electronic stress"[19], i.e. the additional surface stress oscillations induced by the QSE. Using first-principles density functional theory (DFT) calculations, we reveal large quantum oscillations in the surface stress of Pb(111) films as a function of thickness, which adds extrinsically additional strain-mediated quantum oscillations to surface energies of the strained Pb films. Our theory enables

a quantitative estimation of the amount of strain in different experimental samples from the measured stability patterns.

We first briefly introduce the concept of quantum electronic stress that gives rise to quantum oscillations of surface stress. Figure 2.1 illustrates the fundamental difference between the conventional mechanical surface stress and the new quantum surface stress. Consider heteroepitaxial growth of a strained island on surface of thickness d under strain ε due to lattice mismatch, as shown in Fig. 2.1(a). σ^i denotes the intrinsic non-zero surface stress of any given solid surface [20, 21]. In addition, there is a mechanical surface stress induced by misfit strain, which can be calculated as $\sigma^M = \varepsilon E d$ [22], where E is an elastic constant. Then, the total surface stress of the growing film is $\sigma^T = \sigma^i + \sigma^M$. In contrast, consider homoepitaxial growth of an unstrained metal island in the quantum growth regime with strong QSE, as shown in Fig. 2.1(b). There will be no additional mechanical surface stress induced by misfit strain, but instead an additional thickness-dependent quantum surface stress $[\sigma^{QS}(d)]$ induced by QSE. Then, the total surface stress of the growing film becomes $\sigma^T = \sigma^i + \sigma^{QS}$.

Following DFT, the total energy functional of a solid is written as

$$E[n(\vec{r}), \{\vec{R}_m\}] = E_e[n(\vec{r})] + E_{ext}[n(\vec{r}), \{\vec{R}_m\}] + E_I[\{\vec{R}_m\}] \tag{2.1}$$

$E_e[n(\vec{r})]$ is the electronic energy functional of charge density $n(\vec{r})$, including kinetic and electron-electron interaction energy, $E_{ext}[n(\vec{r}), \{\vec{R}_m\}]$ is the ion-electron interaction energy, $E_I[\{\vec{R}_m\}]$ is the ion-ion interaction energy, and $\{\vec{R}_m\}$ are atomic coordinates. Considering a variation of electron density from the ground-state n^0 as $n^* = n^0 + \delta n$ in the absence of strain (i.e., without any lattice deformation); a general expression for lattice stress induced by such pure electronic perturbation or excitation has been recently derived as [19]

$$\sigma_{ij}^{QE} = \frac{1}{V} \int_V \frac{\partial \mu}{\partial \varepsilon_{ij}} \delta n(\vec{r}) d\vec{r}, \tag{2.2}$$

which is called quantum electronic stress. μ is electron chemical potential, $\partial\mu/\partial\varepsilon_{ij}$ is electron deformation potential, and ε_{ij} is strain. In a nanofilm of thickness d,

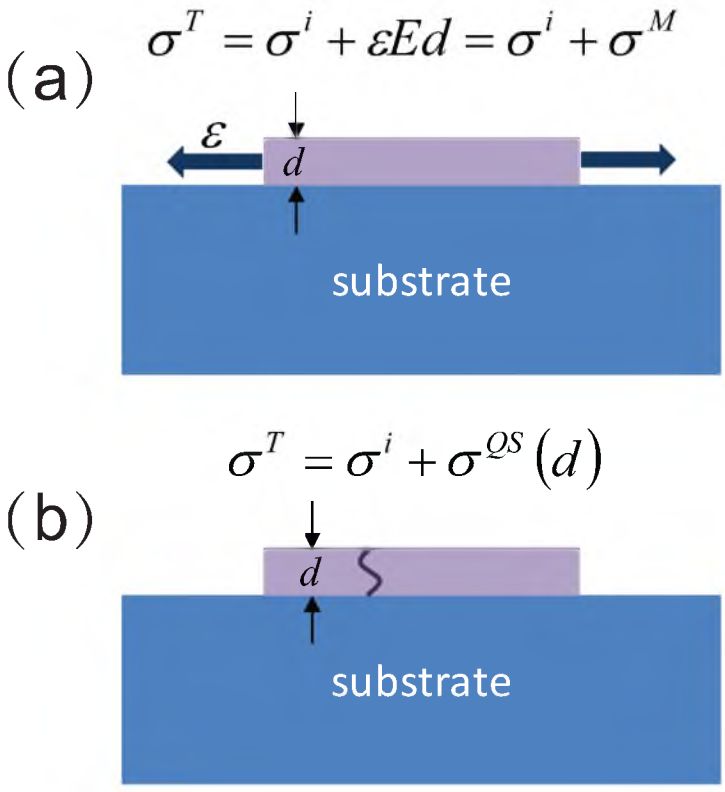

Figure 2.1. Schematic illustration to differentiate the conventional mechanical surface stress induced by misfit strain from the new quantum electronic surface stress induced by QSE. (a) A strained film in heteroepitaxial growth, showing the mechanical surface stress. (b) An unstrained film in homoepitaxial growth, showing the quantum surface stress.

QSE induces variation of charge density and deformation potential along the surface normal z-direction. Then, a special form of quantum electronic "surface" stress can be expressed as

$$\sigma_{ij}^{QS} = \frac{1}{d} \int \frac{\partial \mu}{\partial \varepsilon_{ij}}(z) \delta n(z) dz. \tag{2.3}$$

Note that ε_{ij} is a rank-3 and rank-2 strain tensor in Eq. (2.2) and (2.3), respectively.

We have performed DFT calculations to directly reveal quantum surface stress oscillations in Pb(111) nanofilms. Our calculations are done using VASP code [23] based on density functional theory in plane-wave formalism. For all the freestanding Pb films and Pb film on Si substrate from 1∼11 MLs, ultrasoft pseudopotential [24] and generalized gradient approximation are used with the Pb 5d orbitals included as valence states. For thicker Pb film (12MLs and thicker) on Si substrate, PBE potential [25] and generalized gradient approximation without 5d orbitals are used to save time. All calculations use a plane-wave cutoff of 240eV to obtain good convergence for stresses which typically converge slower than total energy. The Pb film is modeled by a supercell slab with the strain-free film set at the theoretical bulk lattice constant of 5.04Å. The Si substrate was modeled using 6 layers of Si with the bottom two layers fixed at bulk positions and the bottom layer passivated with H. The slabs are separated by a vacuum thickness of >20Å in z-direction, sampled by a 20×20×1 mesh in k-space.

2.3 Results and Discussions

Figure 2.2(a) shows the calculated surface stress (σ), as a function of film thickness (d) up to 130 MLs, of the freestanding strain-free Pb(111) film. It is well-known that surface energy displays an oscillatory dependence on d [4]. What is new is that surface stress σ displays also a strong oscillatory dependence on d. In general, we may also express the surface stress as $\sigma = \sigma^i + \sigma^{QS}(d)$, where σ^i is the mechanical surface stress of a macroscopic thick film which we are familiar with, and σ^{QS} is the new oscillating component of quantum surface stress. The thickness dependence of the quantum surface stress is originated from the thickness-dependent variation of charge density

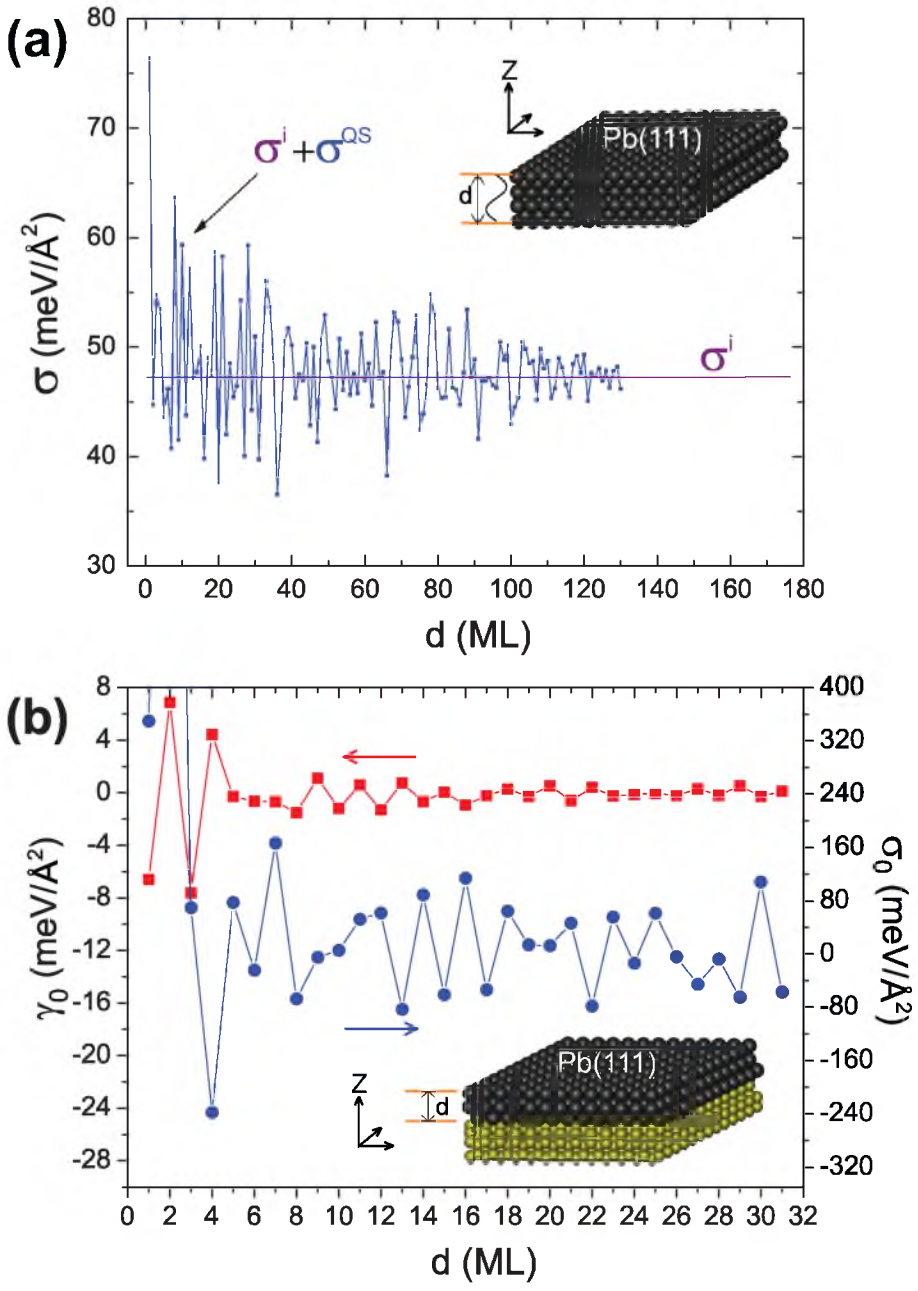

Figure 2.2. Surface energy and surface stress calculation result. (a) Surface stress of freestanding Pb(111) film as a function of film thickness, demonstrating the quantum surface oscillations induced by QSE. (b) Surface energy (squares) and surface stress (dots) of Si-supported unstrained Pb(111) film obtained from DFT calcualtions. The insets show schematics of film.

($\delta n(z)$) and electron deformation potential induced by QSE, as shown in Eq. (2.3). As the film thickness increases, however, σ^{QS} will eventually diminish and σ will converge to σ^i, as indicated by the decreasing oscillation magnitude with increasing thickness in Fig. 2.2(a), although we could not calculate thicker film beyond 130 ML to show full convergence.

In experiments, Pb films are grown on semiconductor substrates, such as Si and Ge. Hence, in order to compare with experiments, we must also include the substrate and interfacial effects. Figure 2.2(b) shows the calculated surface energy γ_0 and surface stress σ_0 as a function of d ranging from 1 to 31 MLs of the strainfree Pb(111) film on a Si substrate (To do so, the Si substrate is strained to match the Pb lattice [5]). For either freestanding or substrate-supported Pb (111) film, we found that both surface energy and stress show an odd-even oscillation modulated by a 9-layer beating pattern; Stress σ_0 displays a larger oscillation magnitude than energy γ_0, and stress converges much slower than energy to the macroscopic value with increasing thickness. Also, the presence of Si substrate causes a phase shift in γ_0 and σ_0 by $\sim$1 ML relative to freestanding film.

We note that QSE induces quantum oscillations in both surface energy and stress, but it should not affect the fundamental relation between energy, stress, and strain. The oscillating quantum surface stress provides a direct link between the QSE and strain effect on the surface energy and hence stability of thin films in the quantum regime. In particular, under a given strain ε, the surface energy will have the following thickness dependence within linear elasticity

$$E(\varepsilon) = E_0(d) + A[\sigma^M + \sigma^{QS}(d)] \cdot \varepsilon. \tag{2.4}$$

In Eq. (2.4), the first term is the surface energy of an unstrained film (denoted by subscript "0") which has a thickness (d) dependence (quantum oscillations) due to the QSE alone. The second term is the strain-induced surface energy via macroscopic surface stress, a constant independent of thickness, while the third term is the strain-induced surface energy via quantum surface stress, which adds extrinsically additional strain-coupled quantum oscillations to surface energy because of the newly discovered

oscillating quantum surface stress. Eq. (2.4) enables a quantitative assessment of the interplay between the QSE and strain effect on the stability of metal nanofilms.

To verify our theoretical framework, we first calculated the surface energies of the 1% strained film as a function of thickness in comparison with the model predictions, as shown in Fig 2.3. We see that the model predictions agree very well with the direct DFT results, validating our theory. Thus, using the DFT calculated surface energies and surface stresses of the "unstrained" film, we can apply our model to predict the surface energy (γ) of the strained film with or without substrate support.

Figure 2.4 (a) and (b) show the predicted surface energy of the freestanding and Si-supported Pb(111) films strained from -3% to 3%, respectively. Strain modifies the surface energy in two important ways. First, strain enhances the QSE by increasing the odd-even oscillation magnitude in γ. This enhancement extends the QSE-induced surface energy oscillations to much thicker films (the oscillation persisting beyond 30 ML with $\sim$3% strain). So, strain provides one possible reason for the experimentally observed stability oscillations existing in much thicker films (>30 ML) [13] than the previous theoretical predictions ($\sim$20 ML) [4]. Second, because the quantum oscillations in surface stress and surface energy are phase shifted, large enough strain will change the oscillation pattern (both the odd-even and beating pattern) of surface energy. This means that strain will alter the relative film stability of different thicknesses. For example, for the strain-free freestanding film, the 14ML film is stable and the 15ML is unstable; however, under 3% strain, the 14ML becomes unstable and the 15ML becomes stable, as shown in Fig 2.4(a).

Experimentally, the observed stability patterns of Pb(111) films grown on Si(111) from different groups are in generally good agreement but with some subtle differences around the nodal points of thicknesses in the beating pattern [13-16]. The reason for such discrepancy remains unresolved, although some general argument has been made by attributing the discrepancy to nonspherical Fermi surface [26] and substrate effect [3,8]. Here, we argue that the discrepancy is partly caused by the different amount of strain in different experimental samples. Below, we apply our model to extract the amount of strain in some experimental samples by matching the predicted stability patterns to the experiments.

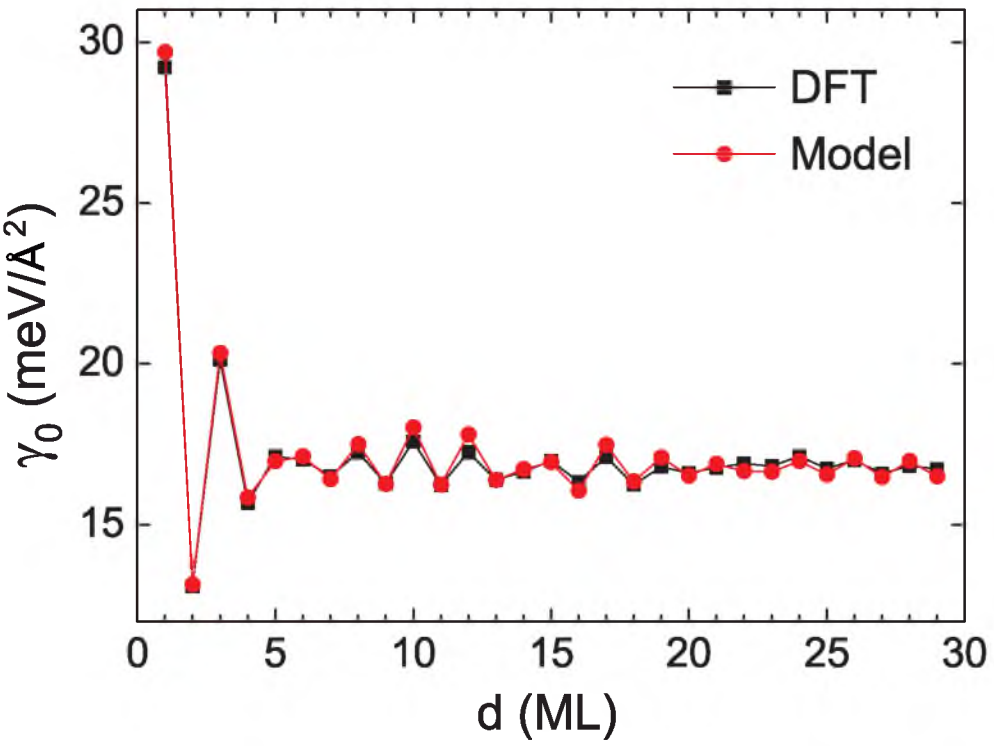

Figure 2.3. Comparison of surface energy between model prediction and direct DFT calculation for a Pb film under 1% strain, showing excellent agreement.

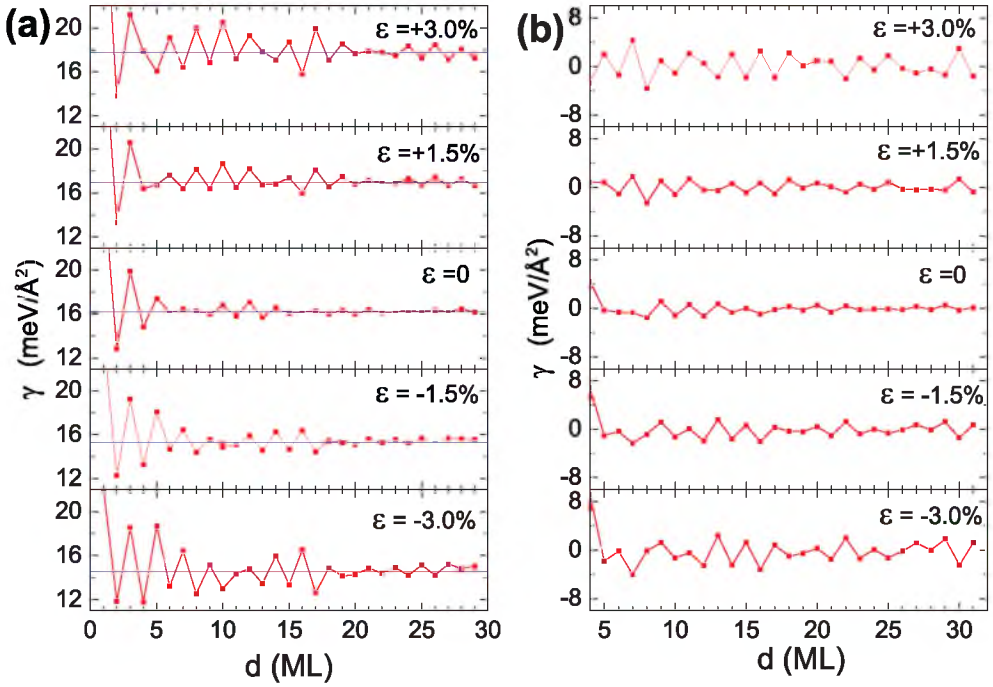

Figure 2.4. Model predicted surface energies of Pb(111) films under strain from -3% to 3%. (a)freestanding film and (b)Si-supported film.

Without strain, the calculated stability pattern from the Si-supported film still agrees poorly with the experiment by Czoschke [13] and Zhang [14], as seen by comparing Fig. 2.2(b) with Fig. 2.5. In particular, both experimental results show large odd-even oscillations from 5 to 8 ML (Fig. 2.5), while the theory shows little oscillation in this region [Fig. 2.2(b)] which is in the vicinity of a nodal point of the beating pattern. To resolve this discrepancy, we apply Eq.(2.4) to predict the stability pattern of "strained" Pb films on the Si substrate, using the calculated surface/interface energies and stresses of the unstrained film on the Si substrate. In fitting the experimental data, we assume a nonuniform strain distribution in the film that decreases linearly with the increasing film thickness [27], and then treat the strain and its decay rate as fitting parameters. We obtained very good fitting results by using a linear strain profile of $1.76\% - (d-5) \times 0.068\%$ for Czoschke's sample [13] and $1.80\% - (d-5) \times 0.061\%$ for Zhang's sample [14], respectively, as shown in Fig. 2.5. Most noticeably, our model correctly predicted the large odd-even oscillations in the range of 5-8 ML as seen in the experiments. This is because there is a large oscillation in the surface stress in this range (see Fig 2.2), which induces additional oscillations in surface energy when strain is applied. The fitted strain is only slightly different in the two samples by $\sim 0.1\%$, in accordance with the overall agreement between the two experimental patterns. Surprisingly, this small difference is enough to account for the subtle differences in the two experimental patterns in the thickness range of 12-14 ML, 21-23 ML, and 30-31 ML, all in the vicinity of nodal points. Overall, the strain is small, less than 2% initially, and decays with the increasing film thickness to less than 1% beyond 10 ML and diminishes around 30 ML. The average strain in a 30 ML film is $\sim 0.9\%$, within the range of general estimation [17].

Recently, Miller *et al.* have shown a fundamental phase relationship between the oscillations of surface energy and of work function in that their beating patterns are always offset by 1/4 of a period [28]. We have shown that the strain can not only change the odd-even oscillations but also shift the phase of beating patterns of surface energy [29]. Applying Miller's phase relation to the Si-supported Pb(111) film by assuming that the interface shifts the work function and surface energy phase together, we can fit the phase of surface energy beating pattern to match (by an offset

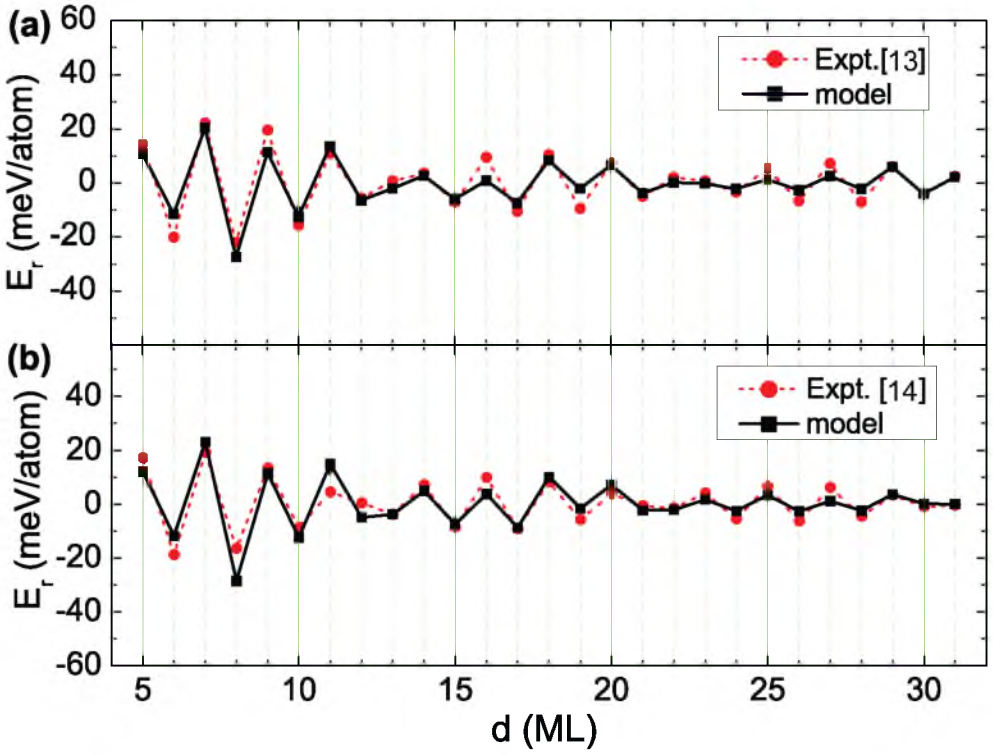

Figure 2.5. Comparison of relative surface energies of Pb(111) film on Si substrate between the experiment (dots) [13, 14] and model prediction with the fitted strain (square).

of 1/4 of a period) the experimental phase of work function pattern, such as the one measured by Qi *et al.* [30], using strain as a fitting parameter. We obtained the best fit with an average 0.75% strain for this particular film, as shown in Fig. 2.6.

2.4 Conclusion

In conclusion, we have developed a theoretical framework to investigate the interplay between QSE and strain effect on the thermodynamic stability of metal nanofilms, through the introduction of a new concept of quantum electronic stress [19]. In the present case, the quantum electronic stress represents the additional quantum oscillations of surface stress induced by QSE. Broadly, our theoretical framework can be extended to investigate the interplay between QSE and strain effect on a range of kinetic and thermodynamic growth properties, such as surface adsorption and diffusion and step-edge barrier, where quantum "adsorption" [31] and "diffusional" stress [32] induced by the QSE can be derived from first-principles to play the role of quantum surface stress here. Thus, our theory will be applicable to both thermodynamic and kinetic properties of nanoscale thin films when QSE and strain effects are prominent.

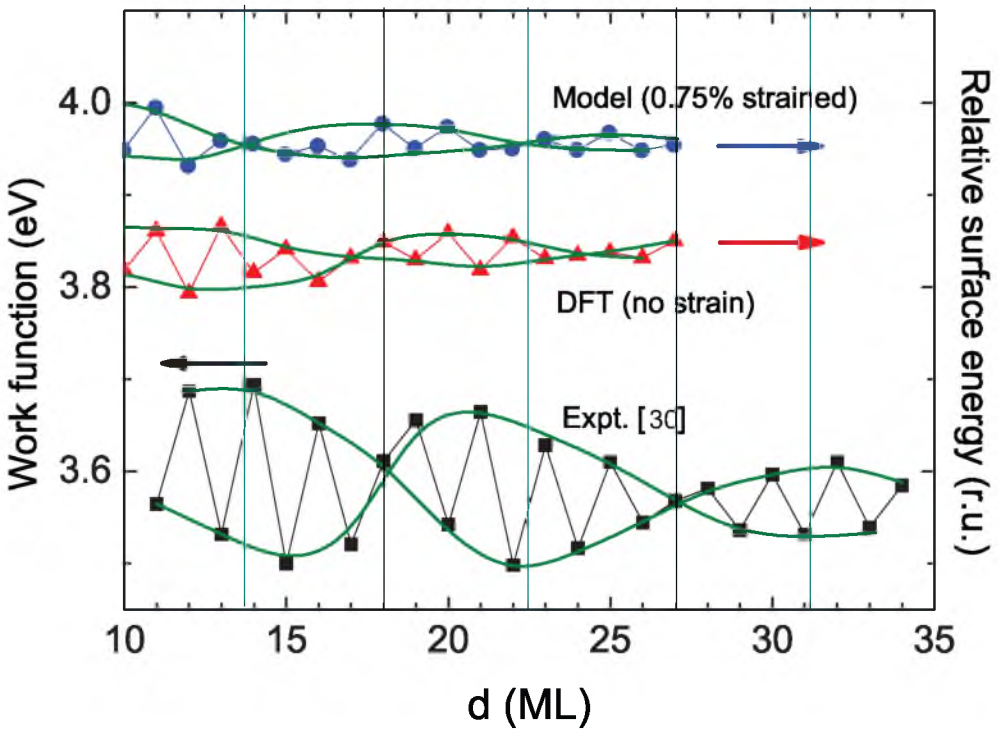

Figure 2.6. Comparison of experimental work function pattern [30] with DFT–calculated surface energy pattern without strain and with model-predicted surface energy pattern with 0.75% strain. Note the 1/4 of a period of phase shift between the experimental data and model prediction.

2.5 References

[1] F. K. Schulte, Surf. Sci. **55**, 427 (1976).

[2] Z. Zhang, Q. Niu, and C.-K. Shih, Phys. Rev. Lett. **80**, 5381 (1998).

[3] V. Yeh, L. Berbil-Bautista, C. Z. Wang, K. M. Ho, M. C. Tringides, Phys. Rev. Lett. **85**, 5158 (2000).

[4] C. M. Wei and M. Y. Chou, Phys. Rev. B **66**, 233408 (2002).

[5] M. H. Upton, C. M. Wei, M. Y. Chou, T. Miller. T.-C. Chiang, Phys. Rev. Lett. **93**, 026802 (2004).

[6] F. Liu and M. G. Lagally, Surf. Sci. **386**, 169 (1997).

[7] F. Liu, Phys. Rev. Lett. **89**, 246105 (2002).

[8] Z. Suo and Z. Zhang, Phys. Rev. B **58**, 5116 (1998).

[9] Y. Jiang, K. Wu, Z. Tang, Ph. Ebert, E. G. Wang, Phys. Rev. B **76**, 035409 (2007).

[10] Z. Kuntova, Z. Chvoj and M. C. Tringides, Euro. Phys. J. B **64**, 61 (2008).

[11] B. Unal, V. Fournee, P. A. Thiel and J. W. Evans, Phys. Rev. Lett. **102**, 196103 (2009).

[12] B. Unal, A. Belianinov, P. A. Thiel and M. C. Tringides, Phys. Rev. B **81**, 085411 (2010).

[13] P. Czoschke, H. Hong, L. Basile, T.-C. Chiang, Phys. Rev. Lett. **93**, 036103 (2004).

[14] Y.-F. Zhang, J.-F. Jia, T.-Z Han, Z. Tang, Q.-T. Shen,Y. Guo, Z. Q. Qiu, Q.-K. Xue, Phys. Rev. Lett. **95**, 096802 (2005).

[15] M. M. Özer, M. Mustafa, Y. Jia, B. Wu, Z. Zhang, H. H. Weitering, Phys. Rev.B **72** 113409 (2005).

[16] Y.-F. Zhang, J.-F. Jia, Z. Tang, T.-Z. Han, X.-C. Ma, Q.-K. Xue, Surface science. **596**, L331 (2005).

[17] H. H. Weitering, D. R. heslinga and T. Hibma, Phys. Rev. B **45**, 5991 (1992).

[18] M. Hupalo, V. Yeh, T. L. Chan, C. Z. Wang, K. M. Ho, M. C. and Tringides, Phys. Rev. B **71**, 193408 (2005).

[19] H. Hu, M. Liu, Z. F. Wang, J. Zhu, D. Wu, H. Ding, Z. Liu, F. Liu, Phys. Rev. Lett. **109**, 055501 (2012).

[20] J. Zang, M. Huang and F. liu, Phys. Rev. Lett. **98**, 14612 (2012).

[21] F. Liu and M. G. Lagally, Phys. Rev. Lett. **76**, 3156 (1996).

[22] H. Hu, H. J. Gao and F. Liu, Phys. Rev. Lett. **101**, 216102 (2008).

[23] G. Kresse and J. Furthmüller, Phys. Rev. B **54**, 11169 (1996).

[24] D. Vanderbilt, Phys. Rev. B **41**, 7892 (1990).

[25] J. P. Perdew, K. Beurke, and M. Ernzerhof, Phys. Rev. Lett **77**, 3865 (1996)

[26] A. Ayuela, E.Ogando and N. Zabala, Phys. Rev. B **75**, 153403 (2007).

[27] M. H. Huang, P. Rugheimer, M. G. Lagally, F. Liu, Phys. Rev. B **72**, 085450 (2005).

[28] T. Miller, M. Y. Chou and T.-C. Chiang, Phys. Rev. Lett. **102**, 236803 (2009).

[29] H. Hong, A. Gray, R. Xu, L. Zhang, T.-C. Chiang, Appl. Phys. Lett. **97**, 241908 (2010).

[30] Y. Qi, X. Ma, P. Jiang, S. Ji, Y. Fu, J.-F. Jia, Q.-K. Xue, S.B. Zhang, Appl. Phys. Lett. **90**, 013109 (2007).

[31] R. pala and F. Liu, J. Chem. physics. **120**,7720 (2004).

[32] D.J. Shu, F. Liu, and X. G. Gong, Phys. Rev. B, **64**, 245410 (2001).

CHAPTER 3

QUANTUM MANIFESTATION OF ELASTIC CONSTANTS IN NANOSTRUCTURES

3.1 Introduction

Mechanical properties of nanoscale solid structures are different from their bulk counterparts. It has been demonstrated experimentally that elastic moduli change their values as a function of the size of nanostructures, such as the diameter of nanorods or thickness of nanoplates [1,2]. The general understanding is that such size dependence of elasticity has its physical origin in the elasticity variation at a material's surface. It is well-known that surface has a different structure from underlying bulk due to bond breaking, surface relaxation, and reconstruction [3-5], which gives rise to excess surface energy and non-zero intrinsic surface stress [3-5]. Consequently, the elastic constants of surface (which may include several atomic layers [4,5]) are distinctively different from those of bulk. In a nanostructure, the surface-to-volume ratio continues to increase with the decreasing size, so that the overall elastic constants of the nanostructure will exhibit a strong size dependence.

There have been many studies about the elastic constants of nanostructures focusing on the surface effect (SS). For example, experiments showed that Young's modulus of a thin film can either increase or decrease relative to bulk when the film thickness approaches nanoscale [6,7]. Theoretically, it is found that the surface could decrease Young's modulus down to 2/3 of its bulk value from calculations using harmonic or Lennard-Jones potential approximation [8,9]. Another calculation found that Young's modulus of thin film varies as the inverse of its thickness, which could go either larger or smaller than the bulk value, based on embedded atom method

(EAM) and Stillinger-Weber potential [10]. EAM simulations of Cu film showed that Cu surface could become either stiffer or softer relative to bulk [11]. In general, elastic constants of nanostructures have been modeled by partitioning the structure into two parts of inner bulk and outer surface with modified surface elastic constants [11-13]. This makes the overall mechanical properties of nanostructures distinctively different from those of their bulk counterpart. For example, the mechanical bending of nanofilms follows the modified Stoney [12] and Timoshenko [13] formula rather than the classical formula for macroscopic thick films.

Besides the SS, it is well-known that there is another effect that becomes increasingly prominent at the nanoscale to affect the properties of low-dimensional nanostructures: quantum size effect (QSE) induced by quantum confinement. When the dimension of a nanostructure is reduced to be comparable to the electron Fermi wavelength, electrons become geometrically confined, giving rise to quantized electronic states that change electronic energy, which in turn modify various properties of nanostructures by QSE, such as surface energy [14], stability [15], and magnetism [16]. Therefore, it is reasonable to expect the QSE to affect the mechanical properties of nanostructures. A few recent theoretical [17-19] and experimental [20] studies have indeed shown the QSE causing quantum oscillations of surface (edge) stress in nanostructures. In general, however, despite the extensive study of the SS on the elastic constants of nanostructures [1,2,6-13], little attention has been paid to the QSE.

In this chapter, we demonstrate quantum manifestations of elastic constants in nanostructures induced by QSE using first-principles calculations. Using Pb nanofilms and graphene nanoribbons (GNRs) as model systems, we show that the Young's modulus and Poisson ratio of nanostructures can display an oscillatory dependence on size, i.e., the thickness of nanofilm and the width of nanoribbon. The main physical origin for such quantum oscillations of elastic constants is the QSE-induced oscillation of electron density inside the nanostructure. Because electron Fermi wavelength is much shorter in a metal than in a semiconductor or insulator, generally, the QSE dominates over the SS in affecting the elastic constants of metal nanostructures, while the reverse is true for semiconductor and insulator nanostructures. It is also important

to point out that previous theoretical studies [8-13] used empirical potentials which did not account for electronic effects. Consequently, the QSE on elastic constants will be missed in these earlier studies even if it were present, which calls for the need of first-principles methods.

3.2 Methodology

Our calculations are carried out using the density functional theory method as implemented in the VASP code [21] with the projector augmented wave method [22] and the Perdew-Burke- Ernzerhof exchange-correlation functional [23]. As shown in Fig. 3.1, Pb(111) film is modeled by a supercell slab set at the theoretical bulk lattice constant of 5.04Å as the reference of a strain-free state [24]. The slabs are separated by a vacuum thickness of 20Å in z-direction, sampled by a 20×20×1 mesh in k-space. GNR is modeled by using a similar super cell technique with a vacuum thickness of 20Å in both y and z directions, sampled by a 10×1×1 mesh in k-space. All calculations used a plane-wave cutoff of 1.3 times of the default VASP value and the structure is optimized until the atomic forces converged to 1 meV/Å. We extracted elastic constants of Yong's modulus (E) and Poisson ratio (ν) from calculating stress-strain relations as a function of system size, for which we varied the Pb(111) film thickness from 1 to 30 monolayers (MLs) and the armchair GNR (AGNR) width from 1 to 29 atomic rows.

Young's modulus describes the stiffness of a material, defined as the ratio of tensile stress over tensile strain ($E = \frac{\sigma_{\parallel}}{\varepsilon_{\parallel}}$). Poisson ratio is defined as the ratio between biaxial transverse compressive strain over longitudinal uniaxial tensile strain ($\nu = -\frac{\varepsilon_{\perp}}{\varepsilon_{\parallel}}$). Here, for Pb(111) thin film, we apply biaxial compressive strain ($\varepsilon_{x,y}$) in the film surface plane (normal to film surface), and calculate the strain-induced film stress in the surface plane ($\sigma_{x,y}$) (note that the intrinsic surface stress in the absence of strain is subtracted) and tensile strain (ε_z) in the surface normal direction. Then, we define the film's Young's modulus as $E_f = \frac{\Delta\sigma_{x,y}}{\Delta\varepsilon_{x,y}}$ and Poisson ratio as $\nu_f = -\frac{\Delta\varepsilon_{x,y}}{\Delta\varepsilon_z}$, as illustrated in Fig. 3.1(a). Similarly, for AGNR, we define $E_r = \frac{\Delta\sigma_x}{\Delta\varepsilon_x}$ and $\nu_r = -\frac{\Delta\varepsilon_y}{\Delta\varepsilon_x}$, as illustrated in Fig. 3.1(b). Another issue for systems with surface and edge is how to define their thickness and width. Here, we use the convention that the thickness

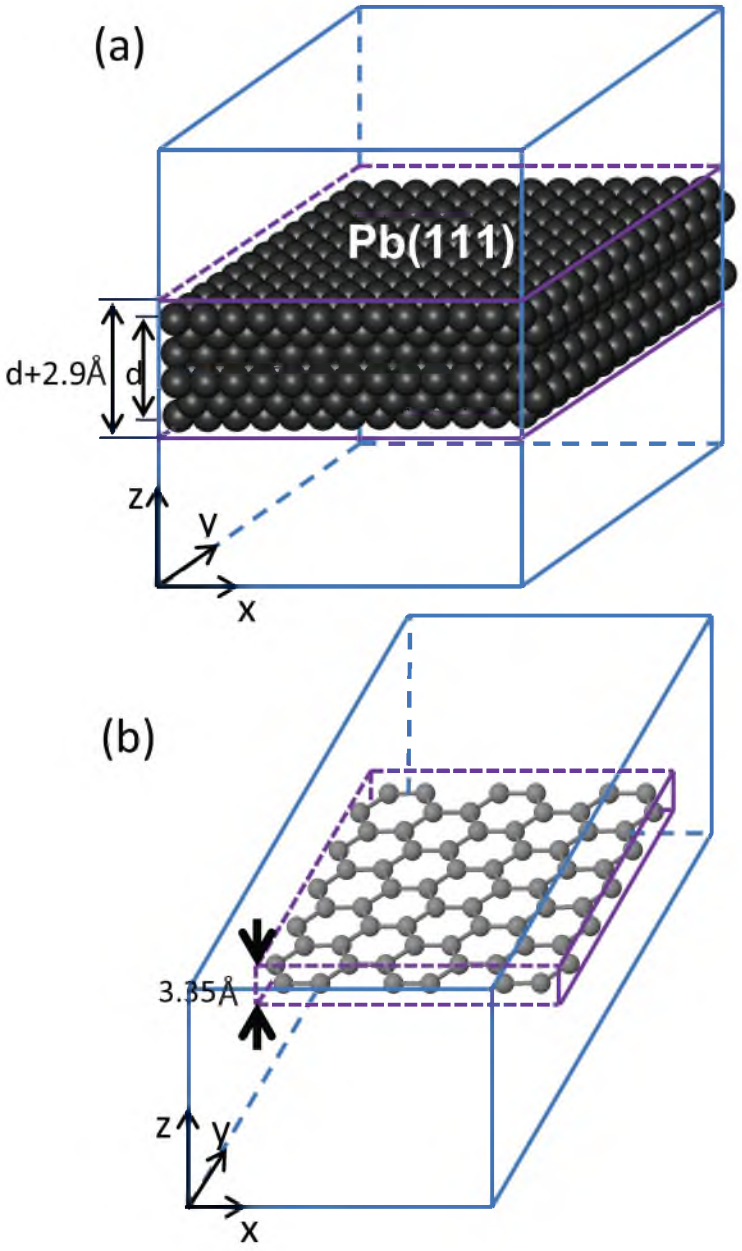

Figure 3.1. Schematic plot of computational supercell of (a) Pb(111) film and (b) armchair GNR. Vacuum region was shown in outer blue box, and the thickness convention is shown in inner purple box.

(width) is set equal to the distance between the two outmost atomic planes (rows) plus one interlayer (inter-row) spacing, as shown in Fig. 3.1(a) [Fig. 3.1(b)]. The interlayer spacing of Pb (111) film is 2.90Å, and the interlayer spacing of armchair GNR is 3.35Å. These same values are used throughout for consistency.

3.3 Results and Discussions

Figure 3.2(a) and (b) shows the calculated E_f and ν_f of Pb (111) film as a function film thickness from 1 to 30 MLs, respectively. Clearly, both E_f and ν_f show a strong odd-even oscillation with a beating pattern period of ~9MLs, manifesting the QSE. Overall, both oscillation patterns are very similar to those of surface energy [25] and surface stress [19] of Pb (111) film. The oscillation amplitude for both E_f and ν_f decays slowly, remaining strong even for ~30ML thick film. Apparently, they differ from the commonly recognized trend that elastic constants change monotonically as a function of film thickness due to SS [8,9,10,11,12,13]. This clearly demonstrates the importance of QSE on modifying the elastic constants of nanofilms.

To better understand the physical origin of quantum oscillations of elastic constants, we may consider a simple free electron gas model. The bulk modulus of a uniform electron gas of density n is [26]

$$B(n) = \frac{\hbar^2(3\pi^2)^{2/3}}{3m} n^{5/3} \propto n^{5/3} \tag{3.1}$$

In a nanofilm, QSE modulates the electron density along the surface normal z-direction. Figure 3.3 shows the charge density distribution $n(z)$ along the z-direction in the 30ML film. Clearly, both the maximum charge density within an atomic plane (n_max) and the minimum density in between two atomic planes (n_min) exhibit an odd-even periodic oscillation originated from the QSE along the z-direction of the film. Thus, approximately, the elastic modulus of the film can be calculated as

$$B_f = \frac{1}{d}\int_0^d B(n,z)dz \propto \frac{1}{d}\int_0^d n(z)^{5/3}dz \tag{3.2}$$

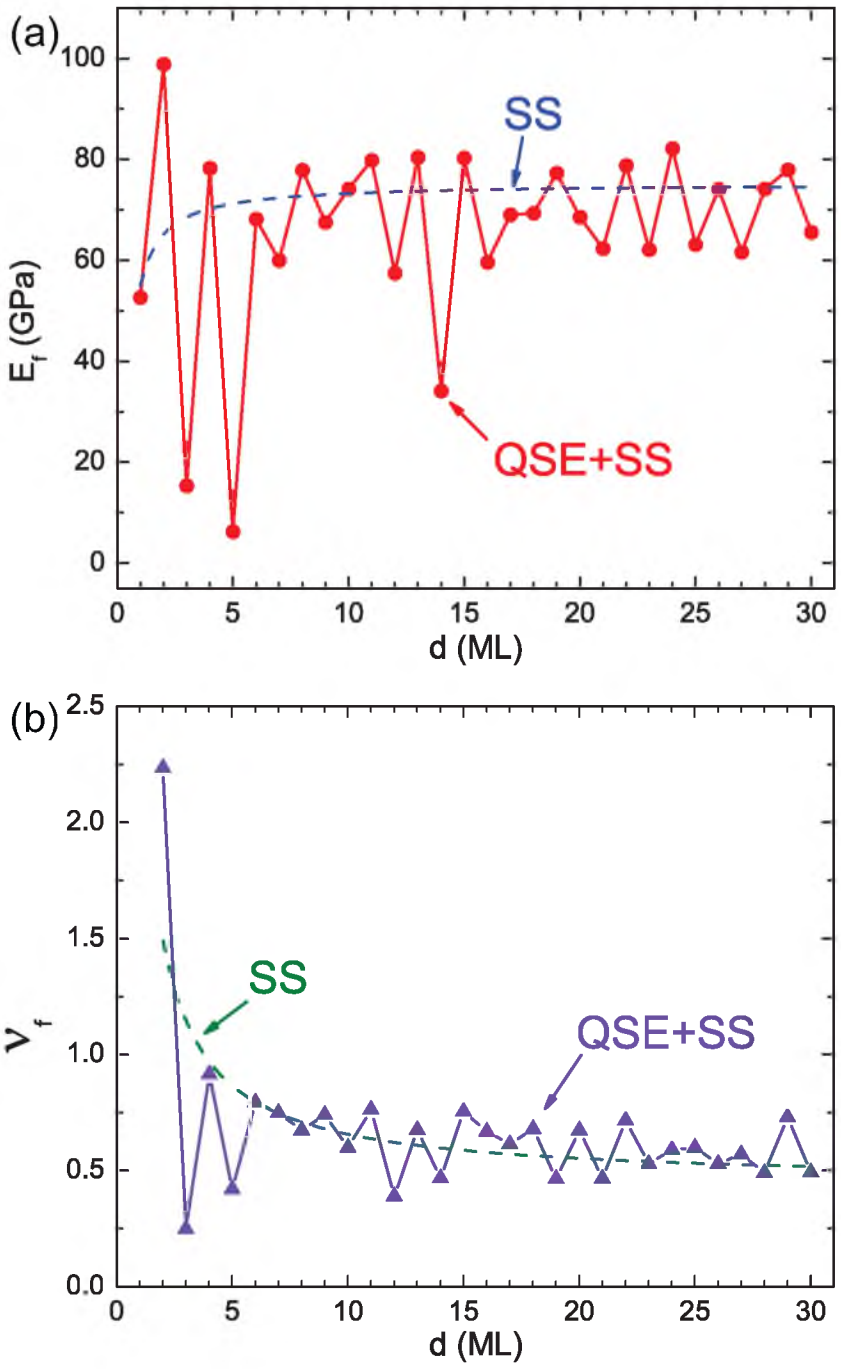

Figure 3.2. DFT calculation result. (a) Young's modulus and (b) Poisson ratio of Pb(111) film as a function of film thickness. The dashed lines show the fitted surface effect on Young's modulus and Poisson ratio.

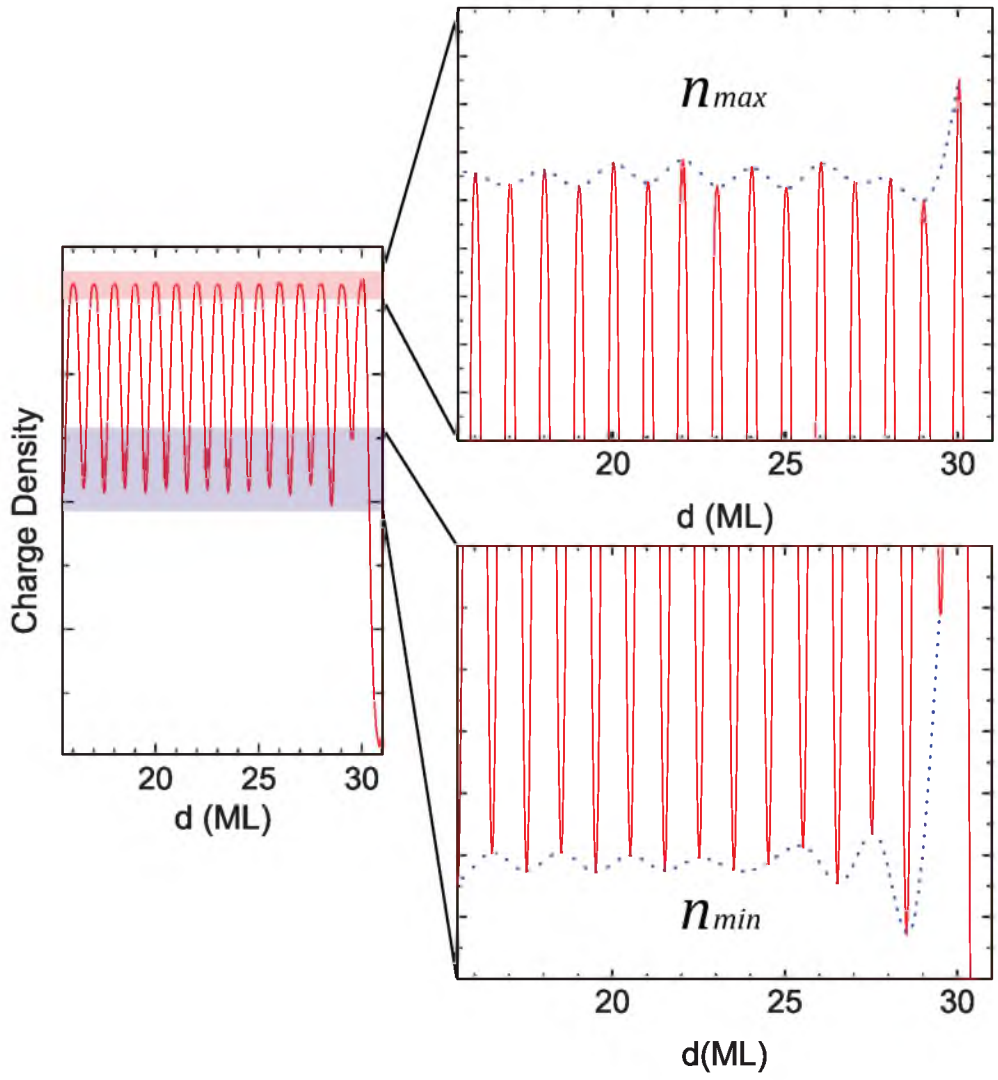

Figure 3.3. Charge density distribution along z-direction of 30ML Pb(111) film. (a) n_{max} shows the maximum charge density within each atomic planes; (b) n_{min} shows the minimum charge density in between atomic planes.

and the QSE-modulated charge density distribution leads to the QSE-modulated film modulus and similarly other elastic constants.

Besides the QSE, the SS should be present also. If one considers the film has an elastic constant (C_b), thickness (d), and a surface layer of thickness (δ) and surface elastic constant (C_s) [12,13], the overall film elastic constant can be easily calculated as

$$C_f = C_b + \frac{2(C_s - C_b)\delta}{d} \tag{3.3}$$

which shows an inverse linear dependence on the film thickness ($\sim 1/d$) [11,12,13]. Whether the surface becomes harder or softer depends on C_s. If $C_s > C_b$, C_f increases with decreasing d; if $C_s < C_b$, C_f decreases with decreasing d. Now, if we pretend to ignore the QSE and use Eq. (3.3) to forcefully fit the calculated E_f and ν_f, we got the black dashed lines shown in Fig. 3.2, which in fact reflect the SS. From the fitting, we obtained E_b ~75 GPa and ν_b ~0.5 at the bulk limit, which are in good agreement with experimental values of 80 GPa and ν=0.4 [27].

For comparison, we also preformed similar calculations for AGNRs. The reason for choosing AGNR is because it has been known that the AGNR exhibits interesting QSE effect in electron band structure [28], with 1/3 being metallic and 2/3 being semiconducting in a three-atomic-raw oscillation as a function of width, as well as similar oscillations in edge energy and edge stress [17] (i.e., equivalent surface energy and stress in 2D). Figure 3.4 shows the calculated Young's modulus (E_r) and Poisson ratio (ν_r) of AGNR as a function of width from 1 to 29 atomic rows. Not too surprisingly, we see the similar quantum oscillations in both E_r and ν_r induced by QSE, with a three-atomic-raw period as in edge energy and edge stress [17]. In addition, we also fit the data using Eq. (3.3) to reveal the edge effect (i.e., the equivalent SS in 2D), shown as the dashed line in Fig. 3.4. From the fitting, we obtained the graphene Young's modulus and Poisson ratio to be 0.95 TPa and 0.16, in good agreement with previous works [29,30].

It is interesting to compare the results of Pb(111) film in Fig. 3.2 with those of AGNR in Fig. 3.4, to reveal the relative importance of QSE versus SS. For

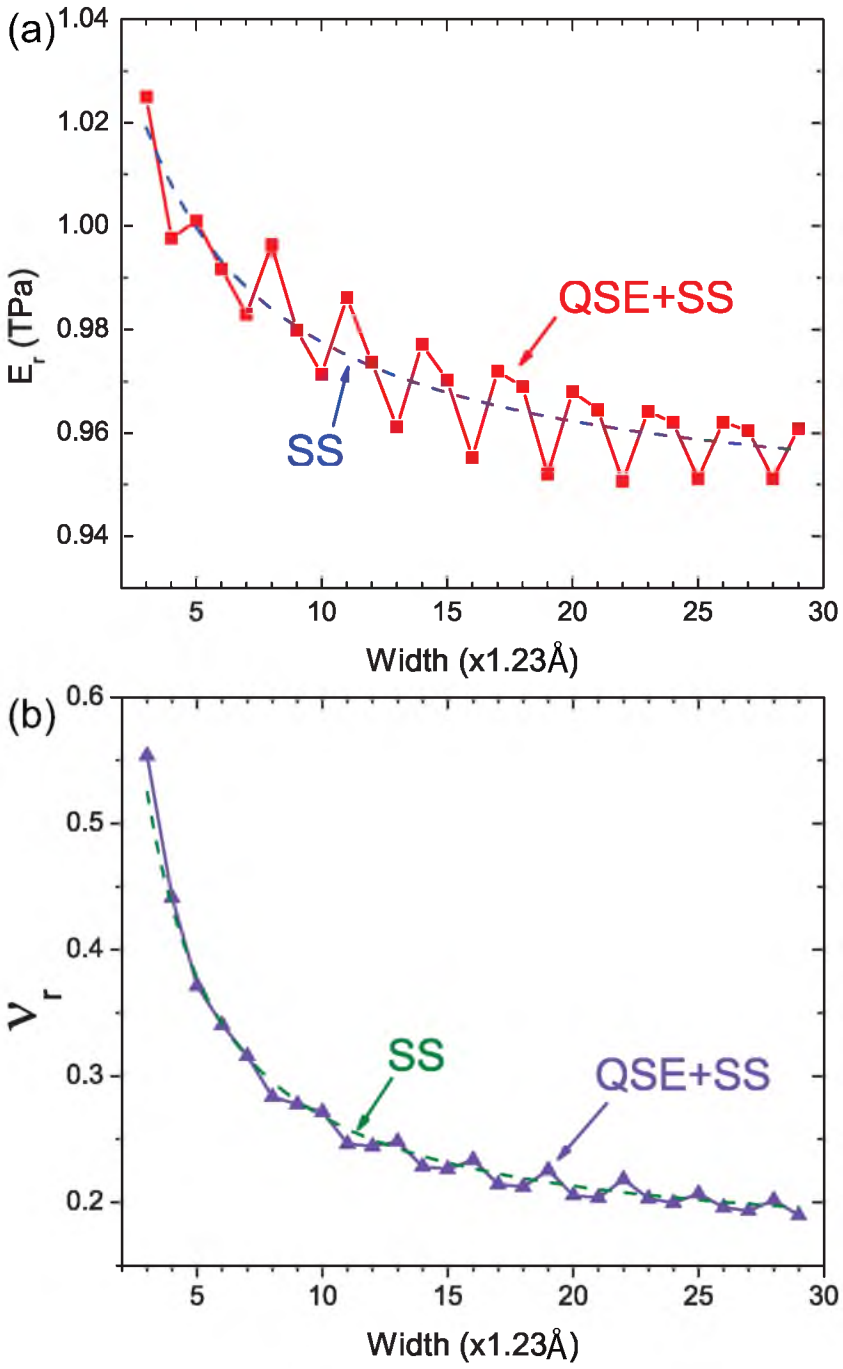

Figure 3.4. DFT calculation result. (a) Young's modulus and (b) Poisson ratio of AGNR as a function of ribbon width. The dashed lines show the fitted surface effect on Young's modulus and Poisson ratio.

film, the QSE modulation of elastic constant is very strong, with an oscillation magnitude changing the elastic constants by ~100%, while the SS is less important, changing the elastic constant by at most ~26%. In contrast, for AGNR, the QSE-induced oscillation magnitude is very small, changing the Young's modulus by a maximum of 2% and Poisson ratio by 11%, respectively, while the edge effect (the equivalent SS in 2D) changes them by as much as 7% and 340%, respectively. Therefore, we conclude that the QSE dominates over the SS in affecting the elastic constants of Pb nanofilms, while the SS dominates over the QSE in affecting the elastic constants of AGNRs. This can be generally understood as follows. First, considering a free electron gas model, the electron Fermi wavelength (λ_F) scales inversely with electron density (n) in a power-law ($\lambda_F \propto n^{-1/3}$ for 3D electron gas and $\lambda_F \propto n^{-1/2}$ for 2D electron gas)[26], so that the Fermi wavelength is usually shorter in metals with a high electron density than in semiconductors and insulators with a low carrier density. Consequently, quantum confinement of electron (the QSE) is stronger in metal nanostructures than in semiconductor and insulator nanostructures. Second, the metal surfaces usually relax or reconstruct less than the semiconductor and insulator surfaces [3], so that the SS is expected to be weaker in metal nanostructures than in semiconductor and insulator nanostructures.

3.4 Conclusion

In summary, we have demonstrated that the QSE can have a profound effect in affecting the elastic constants of nanostructures, with interesting manifestation of size-dependent quantum oscillations, in addition to the monotonic size-dependence induced by SS that has been widely recognized before. Most importantly, we show that for metal nanostructures, the QSE-induced oscillations can be the most dominant effect to completely overwhelm the SS. Our findings shed important new light on our understanding of the mechanical properties of nanostructures by adding interesting quantum aspects to nanomechanics with broad implications.

3.5 References

[1] E.W. Wong, P.E. Sheehan, C.M. Lieber. Science **277**, 1971 (1997).

[2] P. Poncharal, Z.L. Wang, D. Ugarte, W.A. de Heer. Science **283**, 1513 (1999).

[3] F. Liu, M. Hohage, and M.G. Lagally, "Surfaces and Interfaces, Structure of"in "Encyclopedia of Appl. Phys.", eds. H. Immergut and G. Trigg, Supplement Volume, 321-352 (1999).

[4] F. Liu and M.G. Lagally, Phys. Rev. Lett. **76**, 3156 (1996).

[5] J. Zang, M. Huang, and F. Liu, Phys. Rev. Lett. **98**, 146102 (2007).

[6] P. Villain, P. Goudeau, P.O. Renault, and K.F. Badawi, Appl. Phys. Lett. **81**, 4365 (2002).

[7] P.O. Renault, E. Le Bourhis, P. Villain, P. Goudeau, K.F. Badawi, and D. Faurie, Appl. Phys. Lett. **83**, 473 (2003).

[8] C.T. Sun and H. Zhang, J. Appl. Phys. **93**, 1212 (2003).

[9] K. Van Workum and J.J. de Pablo, Phys. Rev. E **67**, 031601 (2003).

[10] R.E. Miller and V.B. Shenoy, Nanotechnology **11**, 139 (2000).

[11] L. G. Zhou and H. Huang, Appl. Phys. Lett. **84**, 1940 (2004)

[12] J. Zang and F. Liu, Nanotechnology, **18**, 405501 (2007).

[13] J. Zang and F. Liu, Appl. Phys. Lett. **92**, 021905 (2008).

[14] K.F. Schulter. Surf. Sci. **55**, 427 (1976).

[15] W. D. Knight, K. Clemenger, W.A. de Heer, W.A. Saunders, M.Y. Chou, and M.L. Cohen, Phys. Rev. Lett. **52**, 2141 (1984)

[16] F. Liu, S.N. Khanna, and P. Jena, Phys. Rev. B **42**, 976 (1990).

[17] B. Huang, M. Liu, N. Su, J. Wu, W. Duan, B.-L. Gu, and F. Liu, Phys. Rev. Lett. **102**, 166404 (2009)

[18] H. Hu, M. Liu, Z.F. Wang, J. Zhu, D. Wu, H. Ding, Z. Liu, and F. Liu, Phys. Rev. Lett. **109**, 055501 (2012).

[19] M. Liu, Y. Han, L. Tang, J.-F. Jia, Q.-K. Xue, F. Liu, Phys. Rev. B **86**, 125427 (2012).

[20] D. Flötotto1, Z. Wang, L.P.H. Jeurgens, and E.J. Mittemeijer, Phys. Rev. Lett. **109**, 045501 (2012).

[21] G. Kresse and J. Hafner, Phys. Rev. B **47**, 558 (1993).

[22] P.E. Blochl, Phys. Rev. B **50**, 17953 (1994); G. Kresse and J. Joubert, Phys. Rev. B **59**, 1758 (1999).

[23] J.P. Perdew, K. Burke, and M. Ernzerhof, Phys. Rev. Lett. **77**, 3865 (1996).

[24] Following the original Gibbs' definition of "excess" surface quantity of the dividing surface of a bulk, surface quantities, including those of nanostructures, should always be defined relative to bulk. For a nanofilm, one may image the film sitting on a substrate. Note that if one fully relaxes the film structure, surface quantities would become ill-defined.

[25] C.M. Wei and M.Y. Chou, Phys. Rev. B **66**, 233408 (2002).

[26] N.W. Ashcroft and N.D. Mermin, Solid State Physics, (Holt, Rinehart, and Winston, New York, 1976).

[27] A.M. James and M.P. Lord, Macmillan's Chemical and Physical Data (Macmillan, London, UK, 1992).

[28] Q. Yan, B. Huang, J. Yu, F. Zheng, J. Zang, J. Wu, B.-L. Gu, F. Liu, and W. Duan, Nano Lett. **7**, 1469 (2007).

[29] K.N. Kudin and G.E. Scuseria, B.I. Yakobson Phys. Rev. B **64**, 235406 (2001).

[30] C. Lee, X. Wei, J.W. Kysar, J. Hone, Science **321**, 385 (2008).

CHAPTER 4

THICKNESS-DEPENDENT ADATOM-ADATOM BINDING ENERGY ON PB(111) FILM: QUANTUM SIZE EFFECT ON ISLAND NUCLEATION

4.1 Introduction

Quantum size effect (QSE) is referred to as an effect manifesting the confinement of electrons in nanostructures whose dimensions are reduced to be comparable to the electron Fermi wavelength [1]. The QSE is expected and shown to alter the intrinsic properties of low-dimensional nanostructures, such as the stability of 0D nanoclusters, reflected by so-called magic numbers [2], the magnetism of 1D nanochains [3], as well as stability [4-8], growth [9], and mechanical properties of nanoribbons and nanofilms [10]. In essence, the quantum confinement introduces discrete electronic states, such as quantum-well states [1] in a nanofilm, redistributing the electron density so as to alter the film total energy and all its associated "bulk" properties. Less transparent but not unexpected is that QSE is also found to alter the energetics of a "foreign" adatom on the surface of a nanostructure, i.e., the interaction between an adatom and nanostructure. This is because quantum confinement changes the surface electron density and hence the surface properties of nanostructures. This has been shown, for example, not only for adatom surface adsorption energy but also for adatom diffusion barrier on surface of nanofilms [11-13].

Now, if we further consider two adatoms on the surface of a nanofilm, as illustrated in Fig. 4.1, and ask a general question of how QSE would affect the interaction between these two adatoms. Because the adatom-adatom binding energy is defined in

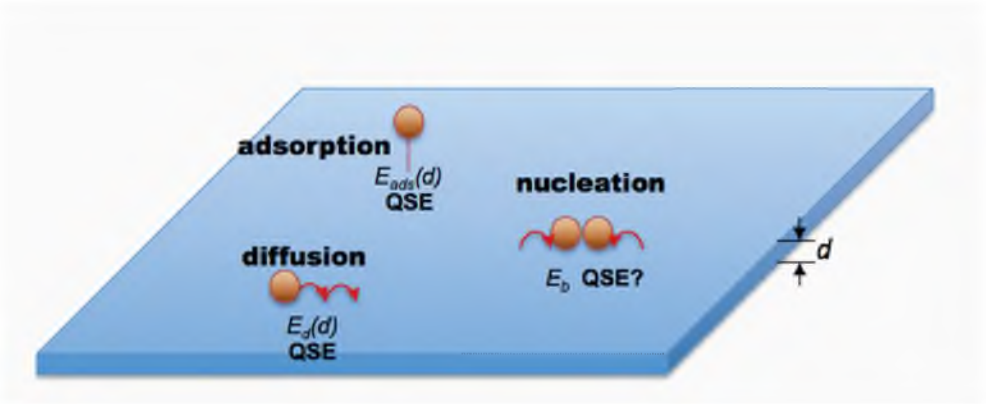

Figure 4.1. Schematic illustration of the adatom surface processes: adsorption, diffusion, and nucleation. Among these three processes, adatom adsorption and diffusion barrier are well known to be affected by QSE, and so is the adatom-adatom binding energy, as we show here.

reference to the energy of isolated adatoms on surface, i.e., adatom surface adsorption energy, there would be an ad-hoc QSE on the adatom-adatom binding energy, even if the QSE will not affect the adatom-adatom interaction. Namely, the adatom-adatom binding energy would show an opposite trend of thickness dependence to that of adatom surface adsorption energy: the lower the adatom surface adsorption energy is, the higher the adatom-adatom binding energy will be. Beyond this ad-hoc effect, however, there could be hidden high-order QSEs changing the adatom-adatom interaction as a function of film thickness, which is the focus of the present study.

One important physical manifestation of adatom-adatom binding energy is island nucleation density on a surface during epitaxial growth [13,15,16]. Island nucleation, defining initial island size, shape, and density, is critical to the subsequent thin film morphology in the later stage of growth. A recent experiment has shown that Fe island density grown on Pb(111) of one thickness is noticeably higher than on another thickness [13]. Another experiment showed that on 4ML Pb(111) film, the Pb island density is ~60 times higher than on 5ML [15]. These observations were explained "solely" by a QSE-induced modulation in adatom surface diffusion barrier (E_d) [13,15,16]. It is generally assumed that the island density (N) scales with diffusion coefficient (D) as $N \sim (\frac{F}{D})^{\frac{1}{3}}$, where F is the deposition flux [13, 15, 16]. Consequently, as D is modulated by QSE, so is N. However, this simple analysis is only valid for cases when critical nucleation size, $i = 1$, so that the adatom-adatom binding does not come into picture. More generally, island nucleation density N will depend on adatom-adatom binding energy (E_b) in addition to diffusion barrier (E_d). Thus, an important question is how the QSE will affect E_b as a function of film thickness, which in turn affects N. Indeed, our first-principles calculations show that island density is not just modulated by the QSE-induced changing adatom diffusion barrier, as commonly perceived before [13,15-16], but also by the adatom-adatom binding energy, when $i > 1$.

4.2 Theory of Island Density

We first review the complete form of island nucleation density equation [17, 18] for the arbitrary value of i,

$$N(i, E_d, \overline{E_b}, T) \propto [\frac{F}{\nu_0} exp(\frac{E_d + \overline{E_b}(i)}{kT})]^{\frac{i}{i+2}} \tag{4.1}$$

Here, $\overline{E_b}(i)$ is the average binding energy per adatom for an island having a size of i adatoms, which should be distinguished from the binding energy of an entire island (E_i) defined in Refs [17] and [18]. From Eq. (1), it is clear that the adatom-adatom binding energy is a key parameter to affect the island nucleation density for $i > 1$. In order to compare directly with experimental data from Refs [15] and [16], we may calculate the ratio of nucleation density on different film thickness (t) as

$$\frac{N_t(i)}{N_{t+1}(i)} = exp(\frac{i\Delta E_d + \overline{\Delta E_b(i)}}{kT} \frac{i}{i+2}) \tag{4.2}$$

In this way, other unknown coefficients and constants in Eq. (1) are eliminated, leaving only three important variables: i, $\Delta\overline{E_b}(i)$, and ΔE_d, where $\Delta E_d = E_{d,t} - E_{d,t+1}$ and $\overline{\delta E_b}(i) = \overline{E_{b,t}}(i) - \overline{E_{b,t+1}}(i)$ are the change of surface diffusion barrier and the change of average adatom-adatom binding energy between the different film thickness, respectively. We stress that the binding energy term is equally important as the diffusion barrier term for any critical nucleation size, except for $i = 1$. We also note that $\overline{\Delta E_d}$ is a constant and only $\overline{\Delta E_b}(i)$ changes with i. So, there are only two parameters, i and $\overline{\Delta E_b}(i)$, altering the island density ratio, as a function of i for the given two film thicknesses.

4.3 Methodology

To quantify the effect of binding energy on the relative island density, we have performed first-principles calculations of $\overline{\Delta E_b}(i)$, for Pb adatoms on Pb(111) film surface as a functional of film thickness from 3 to 5MLs for $i = 2, 3, 4$ and ∞, corresponding to dimer, trimer, tetramer, and a complete overlayer, respectively. Our calculations are carried out using VASP code [19], based on density functional theory in plane-wave formalism. The electron-ion interaction is represented by ultrasoft pseudopotential [20]. Perdew-Burke-Ernzerhof generalized gradient approximation are employed for exchange-correlation potential [21]. All calculations are using a plane-wave cutoff of 240eV to ensure convergence of total energies. The Pb(111) film

is modeled by a 6×6 supercell slab set at the theoretical lattice constant of 5.04Å in the surface x-y plane as before [8,22,23]. The slabs are separated by a vacuum thickness of 20Å in z-direction, sampled by a 6×6×1 mesh in k-space. The Pb slab is fully relaxed first in z-direction to reach the equilibrium geometry before adding adatoms. When depositing adatom on Pb(111) surface, the adatoms are always placed on top of the fcc site, which is energetically more favorable compared to the bcc site based on our calculation, in agreement with previous calculations [11]. We only show the results of the fully relaxed closely packed island shape, as they are found more stable than other less packed island shapes from calculation.

4.4 Results and Discussions

Figure 4.2 (a), (b), and (c) show the island energies for dimer, trimer, and tetramer versus film thickness, respectively. Here, island energy (E_{is}) is defined as $E_{is} = E_{tot} - E_{film}$, where E_{tot} is the total energy of the whole system and E_{sub} is the total energy of the film. Figure 4.2 (d) shows the adatom surface adsorption energy (E_{ads}) as a function of film thickness. In Fig. 4.2, island energy displays a thickness dependence for the same island size i, manifesting QSE. All the islands have higher energies on 5ML than on 3 or 4ML independent of i. For different film thicknesses, the dimer and trimer has the lowest island energy on 4ML (Fig. 4.2a and 4.2b), while the tetramer has the lowest energy on 3ML (Fig. 4.2c). In contrast, the adatom adsorption energy has a different trend and is highest on 5ML (Fig. 4.2d).

There are two separate contributions to the island energy: the binding between the adatoms and film surface in the surface normal direction and the binding in between the adatoms in the direction parallel to surface. By subtracting the adatom absorption energy from island energy, i.e., the isolated adatom-film surface binding energy, we obtain the net adatom-adatom binding energy per atom $[\overline{E_b}(i)]$ within the island on film surface as $\overline{E_b}(i) = (E_{is} - E_{ads}N)/N$. Fig. 4.3 shows the $\overline{E_b}(i)$ for dimer, trimer, and tetramer as a function of film thickness, which represents the critical nucleus size of 2, 3, and 4, respectively [17,18]. Most important to notice is that $\overline{E_b}(i)$ shows a nonmonotonic dependence on Pb film thickness (Fig. 4.3), which does mimic the (opposite) trend of change in adatom absorption energy E_{ads} (Fig.

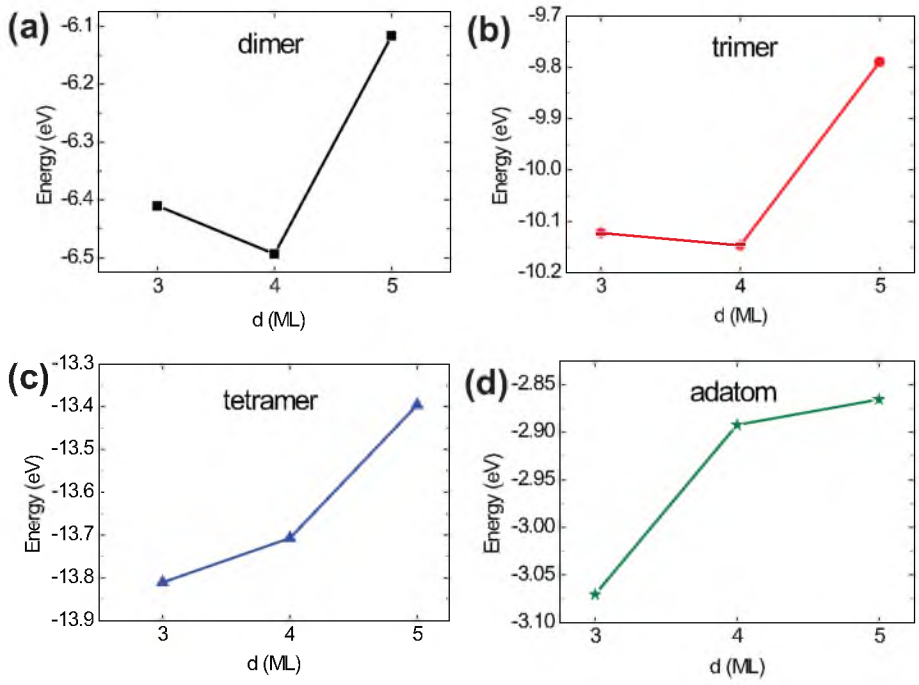

Figure 4.2. Island formation energy for (a) dimer, (b) trimer, (c) tetramer, and (d) adatom absorption energy, as a function of film thickness from 3 to 5 ML.

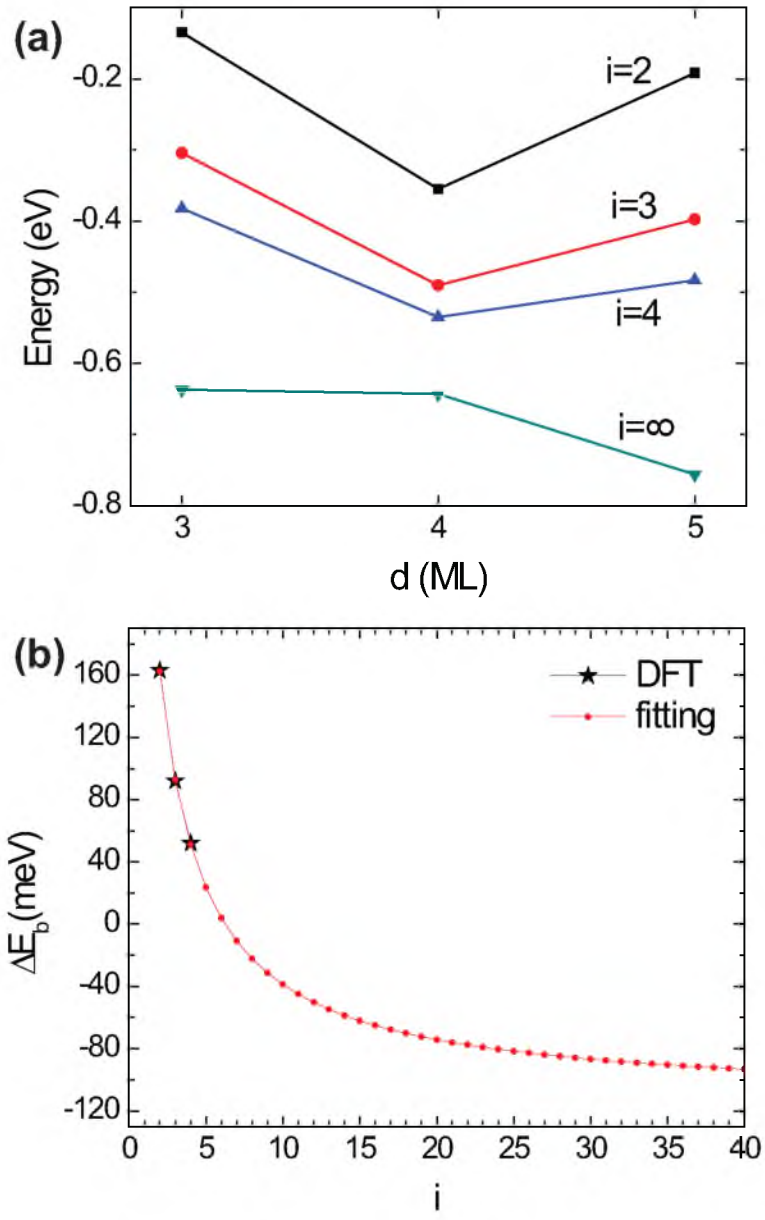

Figure 4.3. Bingding energy of islands. (a) Average adatom-adatom binding energy verses film thickness for i=2,3,4, and ∞. (b) $\overline{\Delta E_b}(i)$ from DFT calculation (pentagram) and fitting (solid dots).

4.2d). The former has a minimum at 4ML, while the latter has a maximum at 5ML. This means that there exists a QSE-induced change of adatom-adatom interaction as a function of film thickness, in addition to the ad-hoc effect of E_{ads}, which contributes to the overall thickness dependence of $\overline{E_b}(i)$. Besides the $\overline{E_b}(i)$ for i =2, 3, and 4, we also calculated $\overline{E_b}(i = \infty)$, which can be deduced from the thin-film energies, as $i = \infty$ corresponds to a complete overlayer. For example, the energy difference between the 5 ML and 4ML film minus the adatom adsorption energy on 4ML gives the $\overline{E_b}(i = \infty)$ on 4ML. The results are also shown in Fig. 4.3.

Next, we discuss the impact of the QSE-modulated adatom-adatom binding energy on island nucleation density. The values of $\overline{E_b}(i)$ on 4ML and 5ML for i = 2, 3, 4, and ∞ are listed in Tab. 4.1. From Fig. 4.3 and Tab. 4.1, we have three important observations: (1) $\overline{E_b}(i)$ decreases with the increasing i for a given film thickness; (2) the change of $\overline{E_b}(i)$ from the 4ML to 5ML film $\overline{\Delta E_b}(i)$ decreases continuously as i increases; (3) the value of $\overline{\Delta E_b}(i)$ is comparable to the change of adatom diffusion barrier E_d, which is calculated to be $E_d = E_{d,4ML} - E_{d,5ML} = 60meV - 30meV = 30meV$ in good agreement with the previous calculation [11]. Notice that $\overline{\Delta E_b}(i)$ gradually decreases with the increasing i, and eventually converges to $\overline{\Delta E_b}(i = \infty) = -113meV$. We can fit $\overline{\Delta E_b}(i)$ nicely with an inverse-linear function, $\overline{\Delta E_b}(i) = 812meV/(i + 0.95) - 113meV$, as shown in Fig. 4.3b. Therefore, we are able to extract the $\overline{\Delta E_b}(i)$ for every island size from the fit. Given ΔE_d and $\overline{\Delta E_b}(i)$, we can now use above equation to assess the relative island density for each i as a function of temperature, and make a direct comparison with experiment. Most importantly, because $\overline{\Delta E_b}(i)$ is comparable to ΔE_d, one has to include the QSE on $\overline{\Delta E_b}(i)$ in addition to Ed in analyzing the QSE on island nucleation density. Previous

Table 4.1. DFT-calculated value of $\overline{E_b}$, $\overline{\Delta E_b}$, and $\Delta E_b + \overline{\Delta E_b}$ for $i = 2, 3, 4$, and ∞.

i	$\overline{E_{b,4ML}}(i)(meV)$	$\overline{E_{b,5ML}}(i)(meV)$	$\overline{\Delta E_b}(i)(meV)$	$\Delta E_b + \overline{\Delta E_b}(i)(meV)$
2	355	192	163	193
3	490	395	92	122
4	535	483	52	82
...	...	...	...	...
∞	643	756	-113	-83

analyses [13,15,16] that considered only the QSE on E_d need to be revisited.

We have drawn Arrhenius plots for the relative nucleation density on the 4ML (N_4) over that on the 5ML film (N_5) versus the inverse temperature for $i = 2$ to 8, as shown in Fig. 4.4. From the Arrhenius plot, we conclude that the ratio of nucleation density is strongly affected by i, with the relative island density decreasing with the increasing i. Particularly, at the experimental growth temperature ($T = 40K$), the relative island density is $N4/N_5 \sim 77$ for $i = 7$, in very good agreement with the experiment having $N4/N_5 \sim 60$ for $i = 8$ [15]. To further illustrate the importance of $\overline{\Delta E_b}(i)$, for comparison, we also purposely make the other Arrhenius plots in Fig. 4.4(b) using the ΔE_d term only and neglecting the $\overline{\Delta E_b}(i)$ term in Eq (4.2), as done in the previous analyses [13,15,16]. This would correspond to the assumption of $i = 1$ or the same $\overline{E_b}(i)$ independent of film thicknesses, namely no QSE on adatom-adatom binding energy, which was of course incorrect, as shown by our direct first-principles calculations above. Comparing Fig 4.4(a) and 4.4(b), we see that the trend is totally reversed. In Fig. 4.4(a), the relative nucleation density increases with the increasing i, while in Fig. 4.4(b), the opposite is true. This indicates that the inclusion of the QSE on adatom-adatom binding energy makes not only a quantitative change of relative nucleation density but also a qualitative difference. We note that from Fig. 4.4(b), one could still make a theoretical fit of experimental data at T=40k, which would give $N4/N_5 \sim 78$ for $i = 2$, differing significantly from experimental value of $i = 8$ [15]. Apparently, such fitting is not physically justified.

4.5 Conclusion

In conclusion, using first-principles calculations, we demonstrate that on the surface of metal nanofilms, the interaction between adatoms is strongly influenced by the QSE to exhibit oscillatory thickness dependence. This has an important physical implication in the theoretical analysis of experimental data of island nucleation density in epitaxial growth. Especially, the island density is not just determined by the manifestation of QSE in surface diffusion barrier, as commonly perceived before, but also in adatom-adatom binding energy. Our finding can be generalized to other low-dimensional nanostructures, where the QSE manifests broadly in the interactions

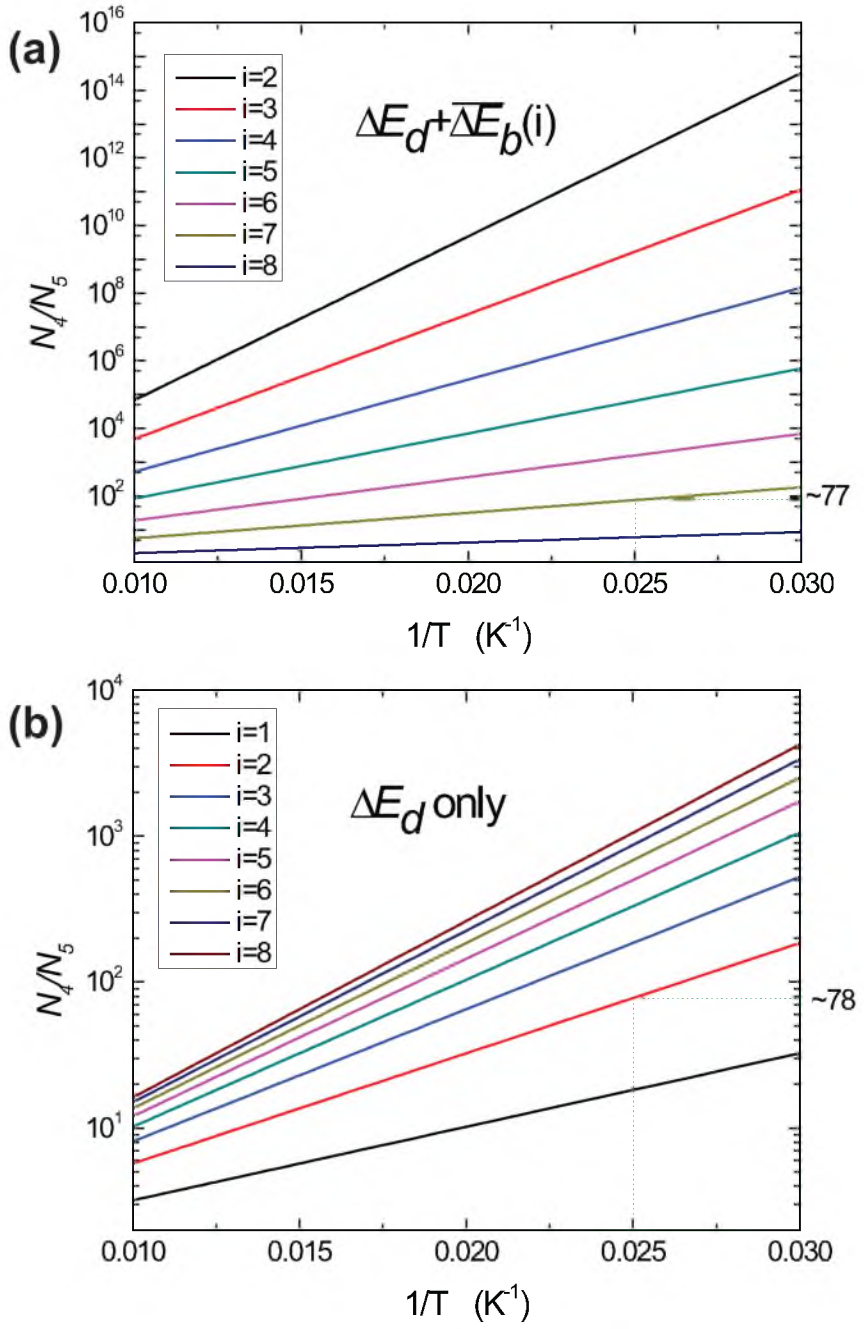

Figure 4.4. Arrhenius plot for relative island density with different i. (a) Both ΔE_d and $\overline{\Delta E_b}(i)$ are included; (b) Only ΔE_d is included while $\overline{\Delta E_b}(i)$ is ignored.

between the adsorbed species on the surface of nanostructures, impacting various surface mediated processes, such as catalytic reactions.

4.6 References

[1] F. K. Schulte, Surf. Sci. **55**, 428 (1976).

[2] W. D. Knight, K. Clemenger, W. A. de Heer, W. A. Saunders, M. Y. Chou, and M. L. Cohen, Phys. Rev. Lett. **52**, 2141 (1984).

[3] F. Liu, S. N. Khanna, and P. Jena, Phys. Rev. B **42**, 976 (1990).

[4] P. Czoschke, H. Hong, L. Basile, and T.C. Chiang, Phys. Rev. Lett. **93**, 036103 (2004).

[5] M. M. Ozer, Y. Jia, B. Wu, Z. Zhang, and H. H. Weitering, Phys. Rev. B **72**, 113409 (2005).

[6] V. N. Piskovoi, E. F. Venger and Y. M. Strelniker, Phys. Rev. B **66**, 115402 (2002).

[7] H. Hu, M. Liu, Z. F. Wang, J. Zhu, D. Wu, H. Ding, Z. Liu, and F. Liu, Phys. Rev. Lett. **109**, 055501 (2012).

[8] M. Liu, Y. Han, L. Tang, J.-F. Jia, Q.-K. Xue, F. Liu, Phys. Rev. B **86**, 125427 (2012).

[9] Z. Zhang, Q. Niu, C.-K. Shih, Phys. Rev. lett. **80**, 5381 (1998).

[10] M. Liu, F. Liu, arXiv:1209.0865 (2012).

[11] T.-L. Chan, C. Z. Wang, M. Hupalo, M. C. Tringides, and K. M. Ho, Phys. Rev. Lett. **96**, 226102 (2006).

[12] S. Li, X. Ma, J.F. Jia, Y.F. Zhang, Q. Niu, F. Liu, D. Chen, P.S. Weiss, and Q.-K. Xue, Phys. Rev. B **74**, 075410 (2006).

[13] L.-Y. Ma, L. Tang, Z.-L. Guan, K. He, X.-C. Ma, J.-F. Jia, Q.-K. Xue, S. Huang, and F. Liu, Phys. Rev. Lett. **97**, 266102 (2006).

[14] Y. Han, M. Hupalo, M. Trangides, and Feng Liu, Surf. Sci. **602**, 62 (2008).

[15] S. M. Binz, M. Hupalo, and M. C. Tringides, Phys. Rev. B **78**, 193407 (2008).

[16] S. M. Binz, M. Hupalo, and M. C. Tringides, J. Appl. Phys. **105**, 094307 (2009).

[17] J. A. Venables, Philos. Mag. **27**, 697 (1973).

[18] J. A. Venables, G. D. T. Spiller, and M. Hanbucken, Rep. Prog. Phys. **47**, 399 (1984).

[19] G. Kresse and J. Furthmller, Phys. Rev. B **54**, 11169 (1996).

[20] D. Vanderbilt, Phys. Rev. B **41**, 7892 (1990).

[21] J. P. Perdew, K. Beurke, and M. Ernzerhof, Phys. Rev. Lett. **77**, 3865 (1996).

[22] C.M. Wei and M.Y. Chou, Phys. Rev. B, **66**, 233408 (2002).

[23] Y. Han, D.-J. Liu, Phys. Rev. B **80**, 155404 (2008).

CHAPTER 5

QUANTUM MANIFESTATIONS OF GRAPHENE EDGE STRESS AND EDGE INSTABILITY: A FIRST-PRINCIPLES STUDY

5.1 Introduction

Graphene, a two-dimensional (2D) single layer of carbon atoms, has attracted tremendous attention because of its unique electronic properties [1] and potential applications in electronic devices [2]. Earlier studies have focused on characterizing the unusual electronic and transport properties of graphene, particularly as a massless Dirac fermion system [1,2]. Some recent attention has been shifted to the structural stability of graphene [2-5]. On the one hand, as a 2D membrane structure, graphene provides an ideal testing ground [3,4] for the classical Mermin- Wagner theorem on the existence of long-range crystalline order in 2D [6,7]. On the other hand, the free edges of graphene are amenable to edge instabilities [5,8-10]. The graphene edge stability is defined by two fundamental thermodynamic quantities: edge energy and edge stress. The edge of a 2D structure can be understood in analogy to the surface of a 3D structure [11,12]: the edge (surface) energy accounting for the energy cost to create an edge (surface) defines the edge (surface) chemical stability; the edge (surface) stress accounting for the energy cost to deform an edge (surface) defines the edge (surface) mechanical stability. First-principles calculations showed that chemically, the armchair edge is more stable with a lower energy, while the zigzag edge is metastable against reconstruction [8]. Empirical-potential calculations showed that both intrinsic edges are under compressive stress, rendering a mechanical edge

twisting and warping instability [10].

Usually, stress and mechanical instability are understood as phenomena of classical mechanics, but they are expected to be affected by quantum effects which become prominent at nanoscale. So far, however, quantum effects have been mostly shown for electronic structure and energetic quantities of low-dimensional nanostructures. Here, we demonstrate an interesting example of quantum manifestations of mechanical quantities in graphene edge stress. Using first-principles calculations, we predict that the armchair edge stress in a nanoribbon exhibits a large oscillation, with ribbon width arising from quantum size effect, while the zigzag edge stress is reduced by spin polarization. Such quantum effects on edge stress in turn manifest in graphene edge mechanical instability, with "quantum" features that apparently cannot be described by empirical potentials or continuum theory.

5.2 Intrinsic Edge Stress of Graphene

Our calculations were performed using the density functional theory (DFT) method as implemented in the VASP code [13]. The supercell technique was adopted to model the graphene nanoribbons (GNR), with a vacuum layer > 15Å. We used a plane-wave energy cutoff of 500 eV and optimized structure until the atomic forces converged to $< 10meV/$Å. The edge energy is calculated as $E_{edge} = (E_{ribbon} - E_{atom})/2L$, where E_{ribbon} is the total energy of the graphene nanoribbon, E_{atom} is the energy per atom in a perfect graphene, and L is the length of edge. The edge stress is calculated as $\sigma_{edge} = \sigma_{xx}/2$, where σ_{xx} is the diagonal component of supercell stress tensor in the x-direction (defined along the edge), which is calculated using the Nielsen-Martin algorithm [14]. All other components of stress tensor vanish. We note that DFT is suitable for calculating ground-state properties of lattice energies and stresses, to which the nonlocal many-body effects are not important.

Figure 5.1 shows the edge energy and edge stress of armchair edges as a function of ribbon width from ∼3.5 to 48Å. One notices that both edge energy and edge stress oscillate with the increasing width having a period of 3 but out of phase with each other. The oscillations are originated from the quantum confinement effect, as seen in the similar oscillations of electron band structures [15-18]. The oscillation of edge

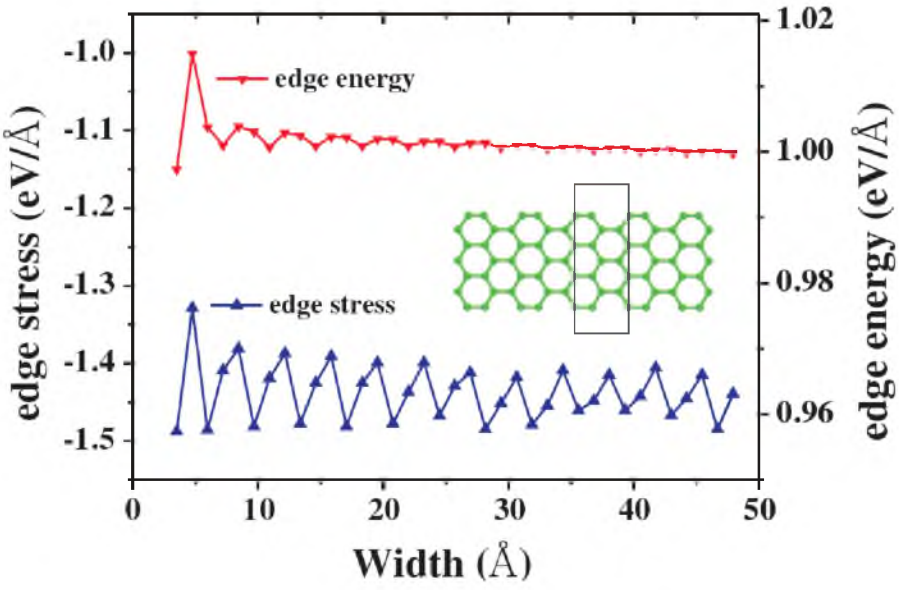

Figure 5.1. The armchair edge stresses and edge energies of graphene nanoribbons as a function of ribbon width. Inset: schematics of the nanoribbon; the rectangle marks one unit cell (supercell) of the ribbon.

energy decays quickly with the increasing width and converges to ~1.0 eV/Å, which agrees well with the previous first-principles values [8]. In contrast, the oscillation of edge stress decays much slower with a mean value of ~ - 1.45 eV/Å (using negative sign as convention for compressive stress). The much larger oscillation in edge stress than in edge energy is possibly caused by the fact that edge stress equals to the derivative of edge energy with respect to strain so that stress is much more sensitive to the width-dependent quantum confinement effect. There is also a slight revival effect in the stress oscillations at ~40Å width, whose origin is not clear and needs further study.

Figure 5.2 shows the edge energy and edge stress of GNR zigzag edges as a function of ribbon width from ~5.0 to 85Å. In this case, both edge energy and edge stress show very weak width dependence and converges quickly, again consistent with their corresponding electronic-structure behavior [15-18]. However, the zigzag edge is known to have an antiferromagnetic (AFM) ground state [17]. The AFM edge energy is calculated to be ~1.2 eV/Å, about 0.2 eV/Å lower than the paramagnetic (PM) edge energy [8,9,19]. Thus, we have calculated the spin dependence of edge stress and found that spin polarization reduces the compressive stress from ~ - 0.7 eV/Å in the PM edge to ~ - 0.5 eV/Å in the AFM edge.

Our first-principles stress calculations confirm qualitatively the recent empirical-potential results [10] that both edges are under compressive stress. However, there are also some significant differences. Two quantum manifestations of edge stress stand out, which are absent from the empirical prediction. One is the quantum oscillation of armchair edge stress, and the other is the spin reduction of zigzag edge stress. The physical origin of edge energy and edge stress is associated with the formation of one dangling bond on each edge atom. The repulsive interaction between the dangling bonds is believed to be one origin for the "compressive" edge stress. In addition, in the armchair edge, it is well-known [20] that the edge dimers form triple -C≡C- bonds with a much shorter distance ~1.23eV/Å (according to our calculation) adding extra compressive stress to the edge, while in the zigzag edge, spin polarization further reduces the compressive stress. Consequently, the armchair edge has a much larger compressive stress ~ - 1.45 eV/Å than the zigzag edge ~ - 0.5 eV/Å, in contrast to

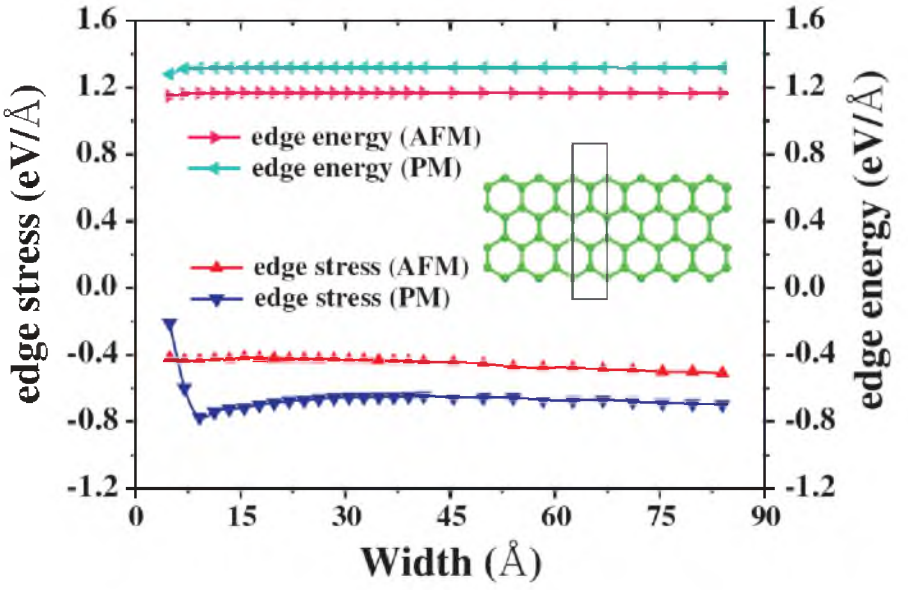

Figure 5.2. The AFM and PM zigzag edge stresses and edge energies of graphene nanoribbons as a function of ribbon width. Inset: schematics of the nanoribbon; the rectangle marks one unit cell (supercell) of the ribbon.

the empirical prediction of a smaller compressive stress in the armchair edge (∼ - 1.05 eV/Å) than in the zigzag edge (∼ - 2.05 eV/Å) [10].

The quantum effects in edge stress will in turn modify the mechanical edge instability. The compressive edge stress means the edge has a tendency to stretch. If we apply a uniaxial in-plane strain to a nanoribbon along the edge direction, the strain energy can be calculated as [10]

$$E_{str} = 2\tau_e L\varepsilon + E_e L\varepsilon^2 + \frac{1}{2}E_s A\varepsilon^2 \tag{5.1}$$

Here, A is the ribbon area, L is the edge length, τ_e is the edge stress, E_e is the 1D edge elastic modulus in a 2D nanoribbon, in analogy to the 2D surface elastic modulus in a 3D nanofilm [21], and E_s is the 2D sheet elastic modulus. Since τ_e is negative, for small enough tensional strain ε (positive), the negative first term (linear to ε) in Eq. 5.1 can always overcome the positive second and third terms (quadratic to ε) to make E_{str} negative. So, the ribbon is unstable against a small amount of stretching along the edge direction. Fitting first-principles calculations, by manually deforming the sheet and ribbon along the edge direction, to Eq. 5.1, we obtained E_s ≈21.09eV/Å^2, E_e(armchair)≈3eV/Å and E_e(zigzag)≈24eV/Å with τ_e already calculated directly (see Figs. 5.1 and 5.2). Our E_s value is in good agreement with the experiment [22] and empirical result [10], but E_e is notably different from the empirical results [10].

Another effective way to stretch the edge of a 2D sheet is by out-of-plane edge twisting and warping motions, which are barrierless processes. For example, assuming a sinusoidal edge warping with displacement $\mu_e = asin(2\pi x/\lambda)$ of amplitude a and wavelength λ, which decays exponentially into the sheet as $e^{-y/l}$ (see inset of Fig. 5.3), where l is the decay length, Shenoy *et al.* have shown that minimization of strain energy leads to characteristic length scales of such warping instability as $l \approx 0.23\lambda$ and $a \approx \sqrt{(-\lambda\tau_e)/(1.37E_b + 14.8E_e/\lambda)}$. Using their empirical-potential values of τ_e, E_e, and E_s, they estimated that the warping magnitude of the armchair edge is smaller than that of the zigzag edge, and both are larger than typical thermal fluctuations [10].

Our first-principles predictions, however, are different in several ways. First, absent from empirical prediction, the quantum oscillation of the τ_e of the armchair edge

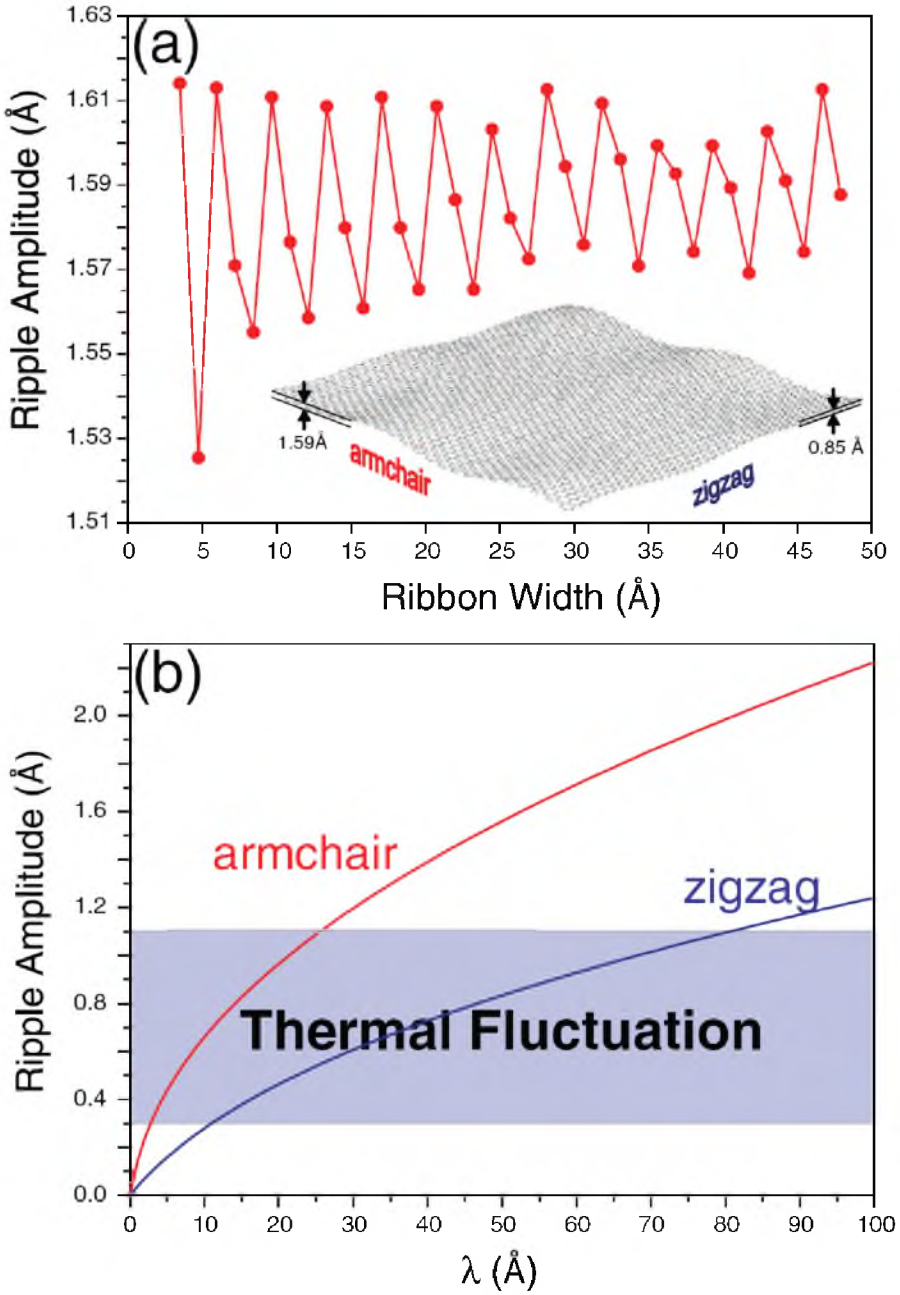

Figure 5.3. Ripple amplitude along graphene edge (a) Armchair edge ripple amplitude versus ribbon width for λ=50Å. Inset: Schematics of ripple formation along the armchair and zigzag edge. (b) Armchair and zigzag edge ripple amplitude as a function of λ. Light blue band shows the typical range of thermal fluctuation.

gives rise to an oscillating armchair edge warping amplitude for a given wavelength as a function of nanoribbon width, as shown in Fig. 5.3(a). Second, the mechanical undulation of zigzag edges induced by compressive edge stress is comparable to thermal fluctuations [3,4], as shown in Fig. 5.3(b), and hence, the two are difficult to distinguish.

Because the compressive edge stress is partly originated from the dangling bond, naturally, we may saturate the dangling bonds to relieve the compressive stress. We have tested this idea by saturating the edge with H that indeed confirmed our physical intuition. For the armchair edge in a 1nm wide ribbon, we found H saturation changes the edge stress from - 1.42 eV/Å to - 0.35 eV/Å; for the zigzag edge in a 2.0nm wide ribbon, it changes the edge stress from - 0.42 eV/Å to + 0.13 eV/Å. Thus, the H edge saturation, or saturation by other molecules in general, is expected to relieve the edge compression and even reverse the compressive stress in a zigzag edge to tensile.

5.3 Edge Reconstruction and Adsorption

Surface reconstruction has long been known as an effective mechanism in relieving surface stress [23]. Thus, we have also investigated possible edge reconstructions in relieving the edge compressive stress. The Stone-Wales (SW) defect [24] appealed to us because a SW defect in 2D is equivalent to a dislocation core in 3D that is known as a common stress relief mechanism. Figure 5.4(a) shows the calculated armchair edge stress along with edge energy as a function of one type of SW defect (7-5-7 ring structure) concentration. Figure 5.4(b) shows an example of the optimized edge structure at the 50% defect concentration. The edge stress increases linearly from compressive to tensile with the increasing SW defect concentration. The most stable edge structure is at ~25% defect concentration where the edge stress is very small and slightly compressive. A small stress value indicates that this chemically stable edge structure (with the lowest edge energy) is also most mechanically stable against deformation.

Figure 5.5(a) shows the ground state AF zigzag edge stress along with edge energy as a function of another type of SW defect (5-7 ring structure) concentration. Figure 5.5(b) shows an example of the optimized edge structure and spin charge density at

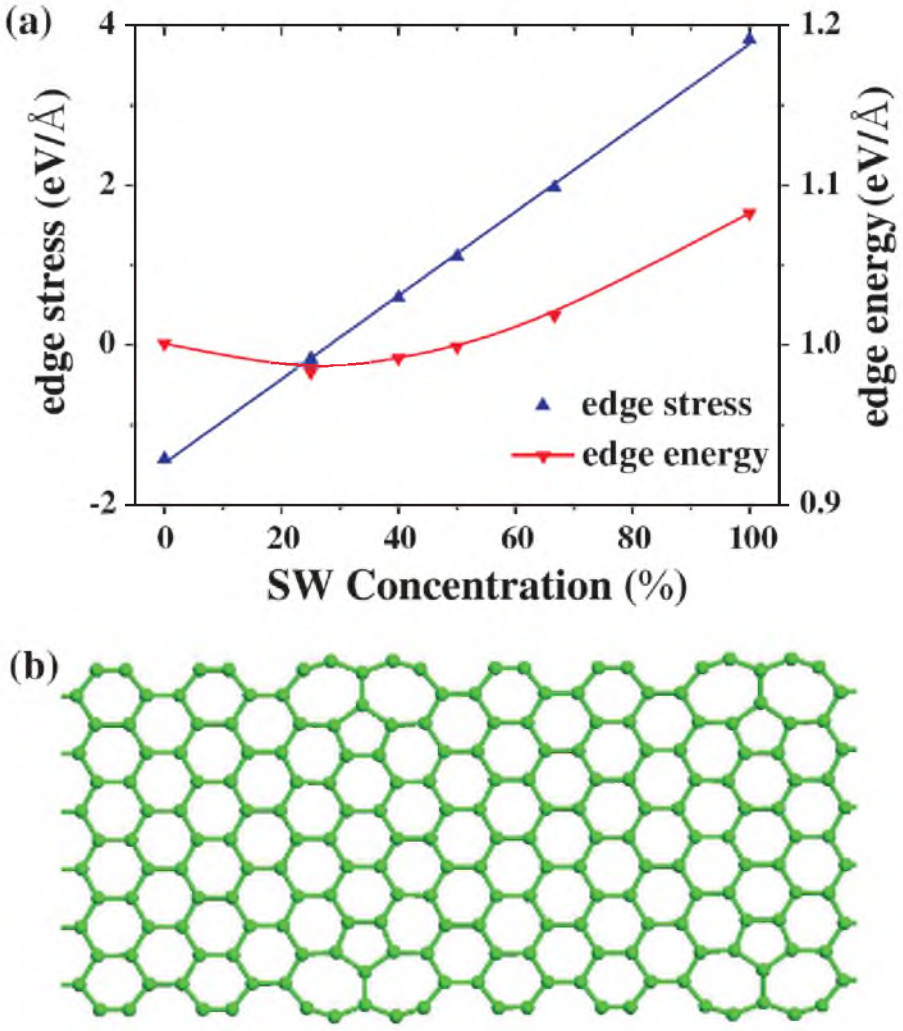

Figure 5.4. Edge reconstruction as a stress relief mechanism: (a) The armchair edge stresses (with linear fit) and edge energies as a function of edge SW defect concentration. (b) The optimized ribbon structure at the 50% SW defect concentration.

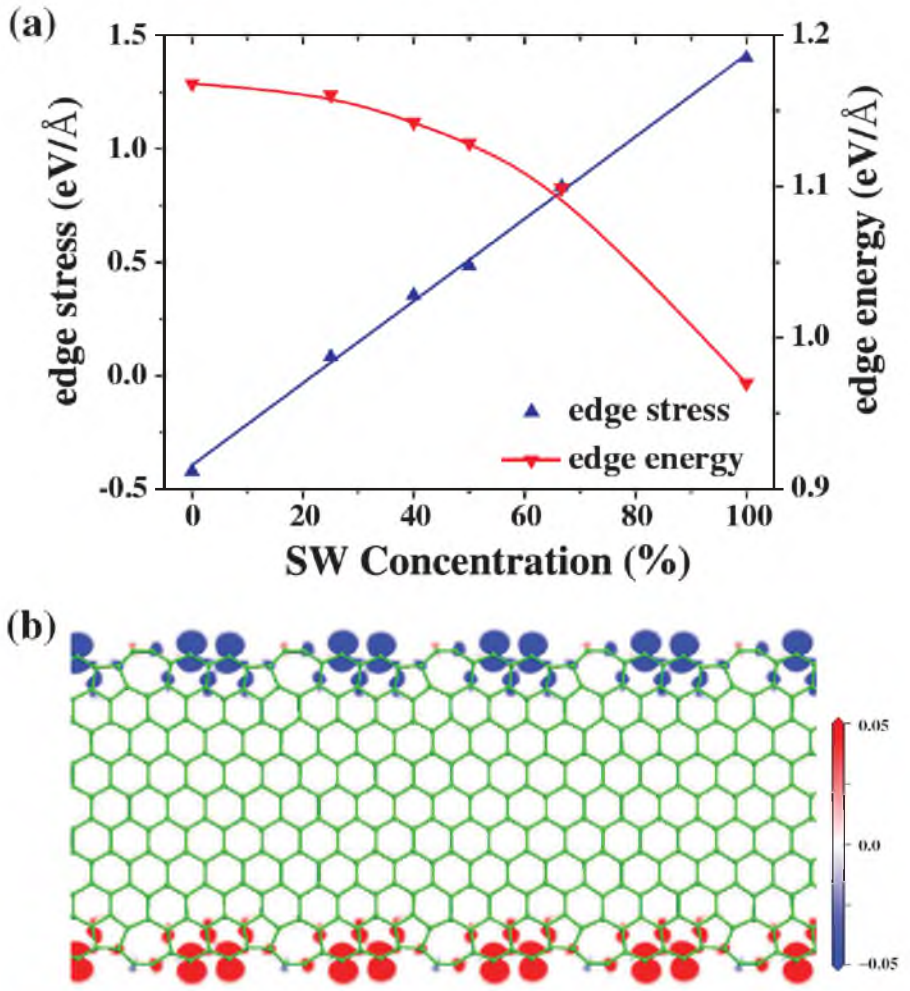

Figure 5.5. Edge reconstruction as a stress relief mechanism: (a) The zigzag edge stresses (with linear fit) and edge energies as a function of SW defect concentration. (b) The optimized ribbon structure and spatial distribution of spin density (charge density difference between spin-up and spin-down states in units of μ_BÅ^{-2}) of the AFM ground state at the 50% SW defect concentration.

the 50% defect concentration. The edge stress increases linearly from compressive to tensile with the increasing defect concentration, the same as the case of the armchair edge [Fig. 5.4(a)], but the edge energy decreases monotonically with the most stable edge having 100% of defects, in agreement with a recent first-principles calculation [8]. The initial compressive edge stress (- 0.5 eV/Å) is completely reversed to a large tensile value of 1.2 eV/Å in the most stable edge. Also, the 100% defected edge becomes non-spin-polarized. In general, the zigzag edge spin decreases continuously with the increasing SW defect concentration, similar to the behavior found previously for other types of defects [25].

5.4 Conclusion

In conclusion, quantum effects have been widely shown for electronic structures and energetic quantities of low dimensional nanostructures. We demonstrate, in addition, quantum manifestations of mechanical quantities in graphene edge stress. We show that quantum confinement can lead to stress oscillations, and spin polarization can reduce stress, which in turn "quantum mechanically" modifies the edge twisting and warping instability.We further show that H edge saturation and SW edge reconstruction can not only improve the "chemical" stability of graphene edges by lowering the edge energy, but also enhance their "mechanical" stability by converting compressive edge stress towards tensile and hence stabilizing the planar edge structure. Our first-principles findings, which cannot be captured by classical methods, provide new insights into the understanding of mechanical stability of graphene. We expect the quantum manifestation of mechanical properties such as stress to exist generally in many low-dimensional nanostructures.

5.5 References

[1] A. H. Castro Neto et al., Rev. Mod. Phys. **81**, 109 (2009).

[2] A. K. Geim and K. S. Novoselov, Nature Mater. **6**, 183 (2007).

[3] J. C. Meyer et al., Nature (London) **446**, 60 (2007).

[4] A. Fasolino, J. H. Los, and M. I. Katsnelson, Nature Mater. **6**, 858 (2007).

[5] M. S. Gass et al., Nature Nanotech. **3**, 676 (2008).

[6] L. D. Landau, Phys. Z. Sowjetunion **11**, 26 (1937).

[7] N. D. Mermin, Phys. Rev. **176**, 250 (1968).

[8] P. Koskinen, S. Malola, and H. Hakkinen, Phys. Rev. Lett. **101**, 115502 (2008).

[9] T. Wassmann et al., Phys. Rev. Lett. **101**, 096402 (2008).

[10] V. B. Shenoy, C.D. Reddy, A. Ramasubramaniam, and Y.W. Zhang, Phys. Rev. Lett. **101**, 245501 (2008).

[11] F. Liu, M. Hohage, and M. G. Lagally, in Encyclopedia of Applied Phys., edited by H. Immergut and G. Trigg, Supplement Vol. **321**, (Wiley-VCH, New York, 1999).

[12] R. Pala and F. Liu, J. Chem. Phys. **120**, 7720 (2004).

[13] G. Kresse and J. Furthmuller, Comput. Mater. Sci. **6**, 15 (1996).

[14] O. H. Nielsen and R. M. Martin, Phys. Rev. B **32**, 3780 (1985).

[15] K. Nakada et al., Phys. Rev. B **54**, 17954 (1996).

[16] K. Wakabayashi et al., Phys. Rev. B 59, 8271 (1999).

[17] Y.-W. Son, M. L. Cohen, and S. G. Louie, Phys. Rev. Lett. **97**, 216803 (2006).

[18] Q. Yan et al., Nano Lett. **7**, 1469 (2007).

[19] H. Lee et al., Phys. Rev. B **72**, 174431 (2005).

[20] T. Kawai, Y. Miyamoto, O. Sugino, and Y. Koga, Phys. Rev. B **62**, R16349 (2000).

[21] J. Zang and F. Liu, Nanotechnology 18, 405501 (2007); Appl. Phys. Lett. **92**, 021905 (2008).

[22] C. Lee et al., Science **321**, 385 (2008).

[23] F. Liu and M. G. Lagally, Phys. Rev. Lett. **76**, 3156 (1996).

[24] A. J. Stone and D. J. Wales, Chem. Phys. Lett. **128**, 501 (1986).

[25] B. Huang et al., Phys. Rev. B **77**, 153411 (2008).

[26] K.V. Bets and B. I. Yakobson, Nano Res. **2**, 161 (2009).

CHAPTER 6

BISTABILITY OF NANOSCALE AG ISLANDS ON SI(111)-(4×1)-IN SURFACE INDUCED BY ANISOTROPIC STRESS

6.1 Introduction

Understanding the shape evolution of stressed/strained islands during heteroepitaxial growth is of great fundamental interest [1-6] as well as practical significance in self-assembly of nanostructures, such as quantum dots [7] and quantum wires [1,8]. One common manifestation is that the growth of a two-dimensional (2D) stressed island [2], or a 3D strained island with fixed height [1], displays a spontaneous shape instability: it adopts a compact isotropic shape at small size and an elongated anisotropic shape beyond a critical size, despite the fact that the island is bounded with isotropic boundary (step) energies and under isotropic stress/strain.

The stress-induced spontaneous shape instability of 2D islands represents a typical case of spontaneous symmetry breaking—transition from a high-symmetry phase to a low-symmetry one, a common phenomenon in nature. (For example, a similar shape transition occurs in carbon nanotubes under pressure [9].) The original theoretical model, as developed by Li, Liu, and Lagally (LLL) [2], has been successfully applied in analyzing various experimental results, including equilibrium shape of 2D island [3], 2D vacancy island [10], surface adsorption pattern [11], surface order-disorder phase transition [12], and elongation of 3D island [13].

One notable feature of the 2D island shape transition, as predicted by the LLL model [2] and confirmed by experiments [10-13], is that the transition from the compact isotropic shape to elongated anisotropic shape is a smooth one as the island

adopts only one type of shape at a given size. This conventional notion, however, has been recently challenged by Zandvliet and van Gastel (ZG) [14], who predicted a bistability in the stress-induced 2D island shape transition. It was shown that compact isotropic islands may coexist with elongated anisotropic islands in the vicinity of critical size if the island is under anisotropic stress, i.e., force monopoles are of opposite directions at neighboring island boundaries. The experimental observation of such bistability, however, can be challenging because it usually occurs in a narrow window of surface stress and island boundary energy conditions [14].

6.2 Experimental Observation

Here, we demonstrate direct experimental evidence for such bistability in stressed Ag nanoislands grown on Si(111)-(4×1)-In surface. First-principles calculations confirm the Ag islands are under anisotropic stress, satisfying the prerequisite condition required by the ZG model. The bistability occurs only at room temperature (RT) growth but not at low temperature (LT), possibly caused by an anisotropic island boundary energy dominating at LT that suppresses the occurrence of the bistability as predicted by the ZG model.

Our experiments were performed in an Omicron scanning tunneling microscope (STM)-molecular beam epitaxy (MBE) combination system under ultra-high vacuum. The base pressure is better than 2.0×10^{-11} Torr. The n-type Si (111) substrates (resistivity of 2-3 Ωcm) with a miscut angle of 0.1° were cleaned by well-established flashing procedures [15], which produced ~200 nm wide terraces separated by monoatomic steps (0.31 nm height). Indium (purity 99.9999%) was deposited from a pyrolytic boron nitride crucible in a Knudsen cell, and large single-domain In(4×1) surface was obtained. Submonolayer Ag (purity 99.9999%) was then evaporated from a tantalum boat at a flux rate of 0.01-0.05 ML/min onto the Si(111)-(4×1)-In surface to grow Ag islands, both at RT and LT (~145 K) cooled by liquid nitrogen flow. For Ag islands grown at LT, the samples were slowly (~1.5 K/min) warmed up to RT for *in situ* STM measurements.

The anisotropic Si(111)-(4×1)-In surface has provided an ideal geometrical template for nanostructure engineering [16-18]. In particular, metal (e.g., Pb and Ag)

islands have been grown on this surface with high uniformity in both island height and width due to the combined quantum size effect in controlling the height and strain effect in controlling the width [16]. The islands are usually elongated along the In chain direction having a transverse periodicity and width equal to the multiple units of the In(4×1) reconstruction [16-18]. Our LT growth shows a conventional behavior, leading to formation of elongated islands with uniform height and width, as seen in previous experiments [16-18]. However, the RT growth shows a nonconventional behavior where both elongated islands and compact islands coexist.

Figures 6.1(a) and 6.1(b) show typical STM images obtained after submonolayer deposition of Ag on the Si(111)-(4×1)-In surface at LT and RT, respectively. Ag islands are randomly distributed on the terraces without concentrating at the step edges. For comparison, the deposition amount and the flux rate of Ag were kept the same at both temperatures. Only elongated Ag nanowires are observed at LT [Fig. 6.1(a)], but both compact nanodots and elongated nanowires form at RT [Fig. 6.1(b)]. In the insets of Figs. 6.1(a) and 6.1(b), the 1D strip structure of the In(4×1) reconstruction is visible surrounding the Ag islands. The Ag nanowires extend along the In chain direction.

To quantify the Ag island size and shape, we collected the statistical distribution of island length l, width w, and height h, and analyzed the dependence of island base aspect ratio ($r = l/w$) on island base size [$D = (lw)^{1/2}$], as shown in Fig. 6.2. At LT, only elongated islands (nanowires) exist [Fig. 6.1(a)]. Figure 6.2(a) shows that the island base aspect ratio increases monotonically with the increasing island size in three branches of data, corresponding to three different island widths covering, respectively, two, three and four rows of In chains (indicated as n = 2, 3, and 4 in Fig. 6.2(a)). The inset of Fig. 6.2(a) shows that most nanowires have a height of 4-6 atomic monolayer (ML). At RT, both elongated islands (nanowires) and compact islands (nanodots) coexist [Fig. 6.1(b)]. Figure 6.2(b) shows that the nanodots have a constant base aspect ratio of r $\sim$ 1 (as expected), while the nanowires' base aspect ratio increases monotonically with the increasing island size in two branches, corresponding to n = 2 and 3. The inset of Fig. 6.2(b) shows that the nanodots have a broad height distribution peaked at $\sim$14 ML, while the nanowires have predominantly a height of

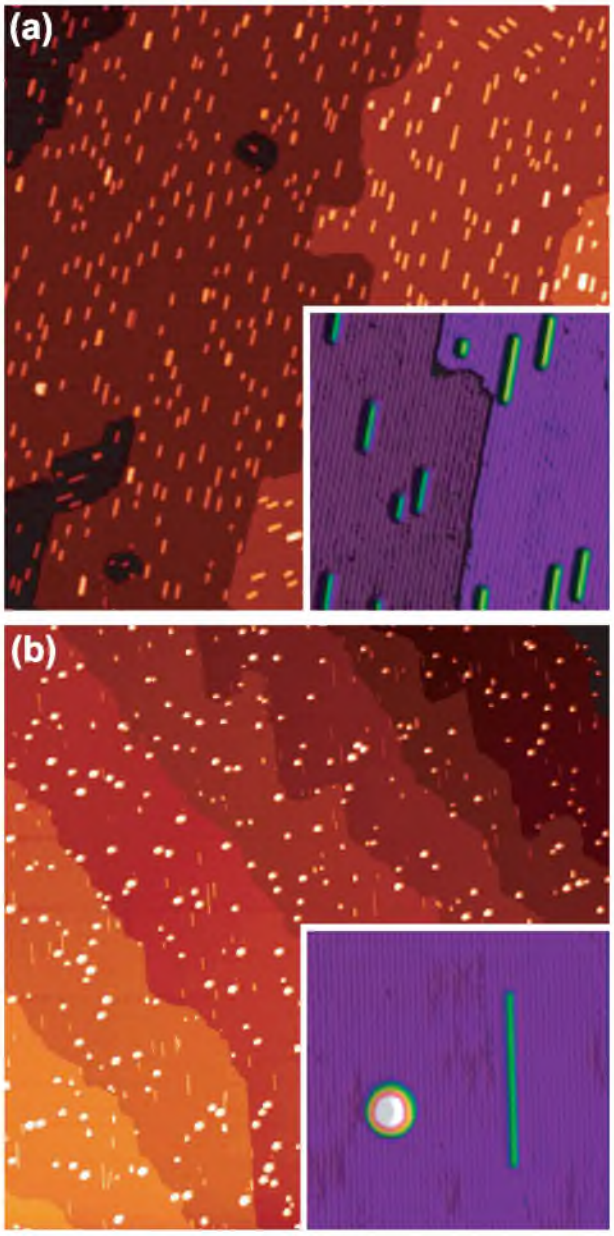

Figure 6.1. Experimental results: (a) Large-scale (381×381 nm^2) STM image of Ag islands grown on the Si(111)-(4×1)-In surface at LT. Only elongated islands exist. Inset: High resolution STM topography (64×64 nm^2) of Ag nanowires. (b) Large-scale (1270×1270 nm^2) STM image of Ag islands grown on the Si(111)-(4×1)-In surface at RT. Both round and elongated islands coexist. Inset: High resolution STM topography (64×64 nm^2) of a Ag nanodot and a Ag nanowire. The nanowires in the insets of (a) and (b) occupy two In chains whose period in the transverse direction is 1.33nm. All images were acquired at $V_{tip} = -2.0V$, $I = 20pA$.

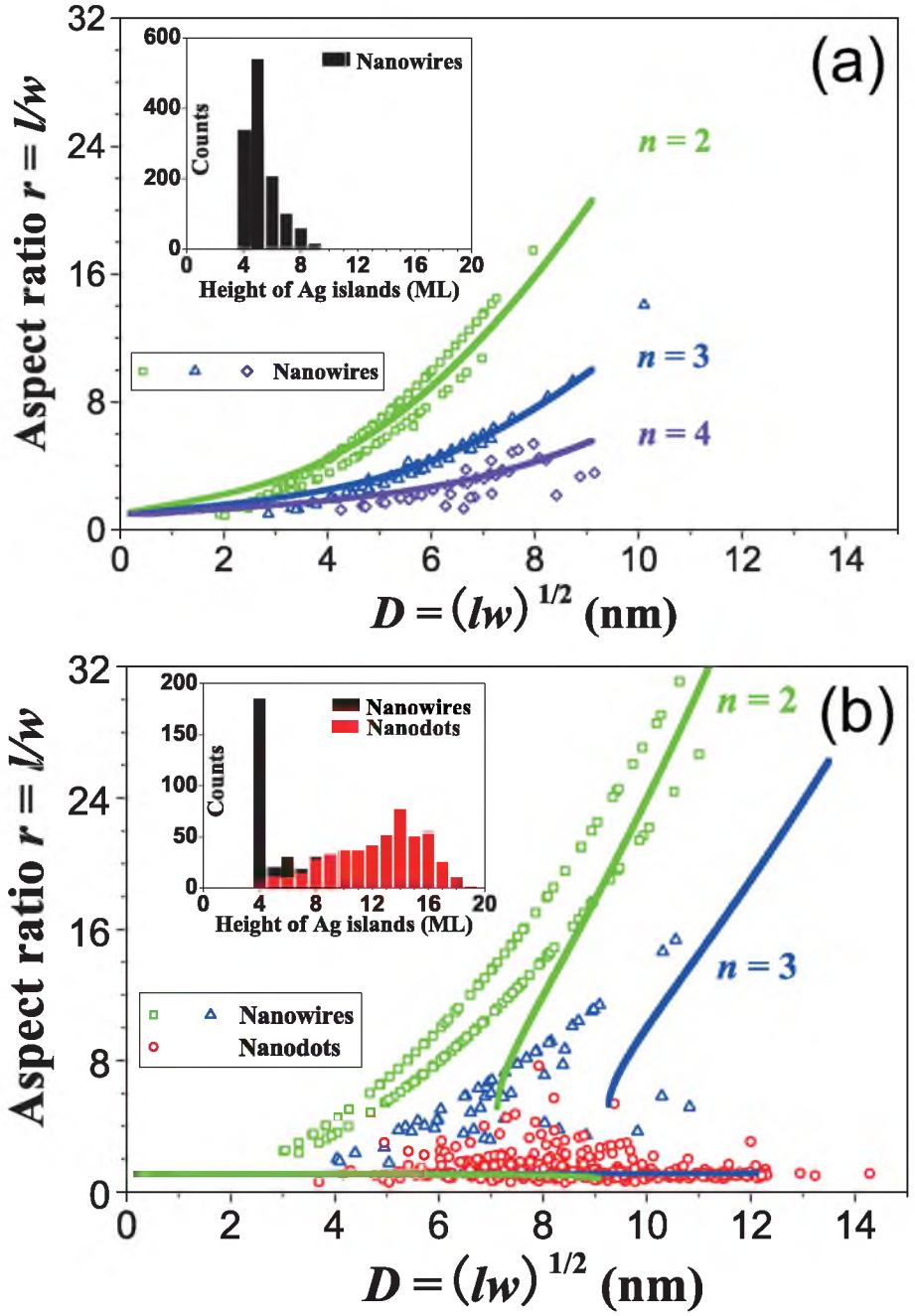

Figure 6.2. Statistical distribution of island shape and height: (a) Dependence of the aspect ratio on the root of Ag island area in the LT experiments (total 1852 Ag islands are sampled). The points corresponding to Ag nanowires densely distribute along the branches n = 2, 3, and 4 (green, blue, and violet parabolas, respectively). it indicates that the numbers of In chains occupied by the nanowires are mainly $n = 2$, 3, and 4. Inset: The height distributions of Ag nanowires in the LT experiments. (b) Dependence of the aspect ratio on the root of Ag island area in the RT experiments (total 703 Ag islands are sampled). The branches $n = 2$, 3 fit the points corresponding to Ag nanowires (black squares) and Ag nanodots (red circles). Inset: The height distributions of Ag nanowires and nanodots in the RT experiments.

4 ML.

6.3 Theoretical Analysis

The intriguing experimental results as shown in Fig. 6.2 have several important implications. Thermodynamically, the observed increase of island aspect ratio with increasing island size implies a stress-induced (strain-induced) growth shape evolution [1,2]. The monotonic increasing aspect ratio, without undergoing a transition from compact to elongated shape at a critical size, indicates an anisotropic island boundary energy which removes the criticality of the strain-induced island shape instability, as predicted by the LLL model [2]. (Anisotropic island boundary energy alone would induce an anisotropic equilibrium island shape of fixed aspect ratio independent of island size.) The islands elongate selectively along the In chain direction, which is caused by anisotropic island boundary energy and/or anisotropic strain [8], consistent with the fact that these islands are grown on a highly anisotropic Si(111)-(4×1)-In template surface. The most interesting observation, however, is the coexistence of compact and elongated islands at RT which is believed to be the first experimental evidence supporting the recent ZG model prediction of bistability of strained islands [14]. Kinetic arguments may explain the continuous elongation with increasing island size, but not the coexistence of both island shapes. We note that for each island shape, there can be multiple stable island sizes, or more specifically, the island widths defined by the template surface reconstruction. However, it is the stress-induced bistable island shape occurring for each stable island width that is the central physical question to be answered below by analyzing the island shape evolution with the ZG model.

The stress-induced island bistability as predicted by the ZG model can only occur under certain growth conditions. The most stringent condition is that the island must be stressed in such an anisotropic manner that force monopoles at neighboring island boundaries point to the opposite directions. Therefore, to confirm this hypothesis, we performed first-principles calculations to determine the stress state of the Ag island on the Si(111)-(4×1)-In surface.

Our calculations were done using the VASP code [19] with options of local density approximation, projector-augmented wave pseudopotentials, and conjugate gradient

method for atomic structural relaxation. We use the supercell of slab to model both the Si(111)-(4×1)-In surface and the Ag film on the surface with a 10 Åvacuum layer, as shown in Fig. 6.3. We used an energy cut-off of 300 eV. The Si substrate is set at the theoretical lattice constant of 5.408 $\AA$ and the initial atomic positions of (4×1)-In reconstruction [Fig. 6.3(a)] are set up following Ref. [20].

We used an orthorhombic supercell with cell vectors specifically chosen having x-axis perpendicular to the In chain direction and y-axis parallel to the In chain direction, i.e., the directions of principal axes, so that surface stress tensor will have only the non-zero diagonal components [21]. For the clean Si(111)-(4×1)-In surface, we used a supercell size of 13.246 Å× 3.824 Å× 40.0 Å[Figs. 6.3(a) and 6.3(b)] and a special k-point grid of 3 × 9 × 1 to sample its Brillouin zone. We obtained the stress of the Si(111)-(4×1)-In surface as $\sigma^s_{xx} = 0.159 eV\AA^{-2}$, $\sigma^s_{yy} = 0.120 eV\AA^{-2}$.

For the Ag film covered Si(111)-(4×1)-In surface, it has been shown that five Ag atomic rows may cover one period of the (4x1) surface in the direction perpendicular to the In chain (four Si lattice in this direction), and four Ag atomic rows cover three periods of Si lattice to minimize the lattice mismatch between Ag and Si in both directions [18]. Based on this model, we added four Ag MLs in accordance to the most favorable island height observed in the experiments (see insets of Fig. 6.2). We used a supercell size of 13.246 Å× 11.471 Å× 54 Å[Figs. 6.3(c) and 3(d)] and a special k-print grid of 3 × 3 × 1 to sample its Brillouin zone. We obtained the stress of the Ag film on Si(111)-(4×1)-In as $\sigma^f_{xx} = 0.119 eV\AA^{-2}$, $\sigma^f_{yy} = 0.149 eV\AA^{-2}$.

Using the above surface stress tensors, it is then straightforward to calculate the force monopoles along the Ag island boundaries on the Si(111)-(4×1)-In surface, as shown in Fig. 6.4, with $F_x = \sigma^f_{xx} - \sigma^s_{xx} = -0.04 eV\AA^{-2}$, $F_y = \sigma^f_{yy} - \sigma^s_{yy} = 0.029 eV\AA^{-2}$. The different sign means that the force monopoles at the Ag island boundary point inward in the direction along the In chain, but outward in the transverse direction, as illustrated in Fig. 6.4. So, indeed, we found that the force monopoles at the Ag island neighboring boundaries point to the opposite directions, satisfying the mandatory condition for the occurrence of bistability predicted by the ZG model.

Using the calculated force monopoles, we now try a theoretical fitting to each branch of experimental data of different island width in Fig. 6.2, using the LLL and

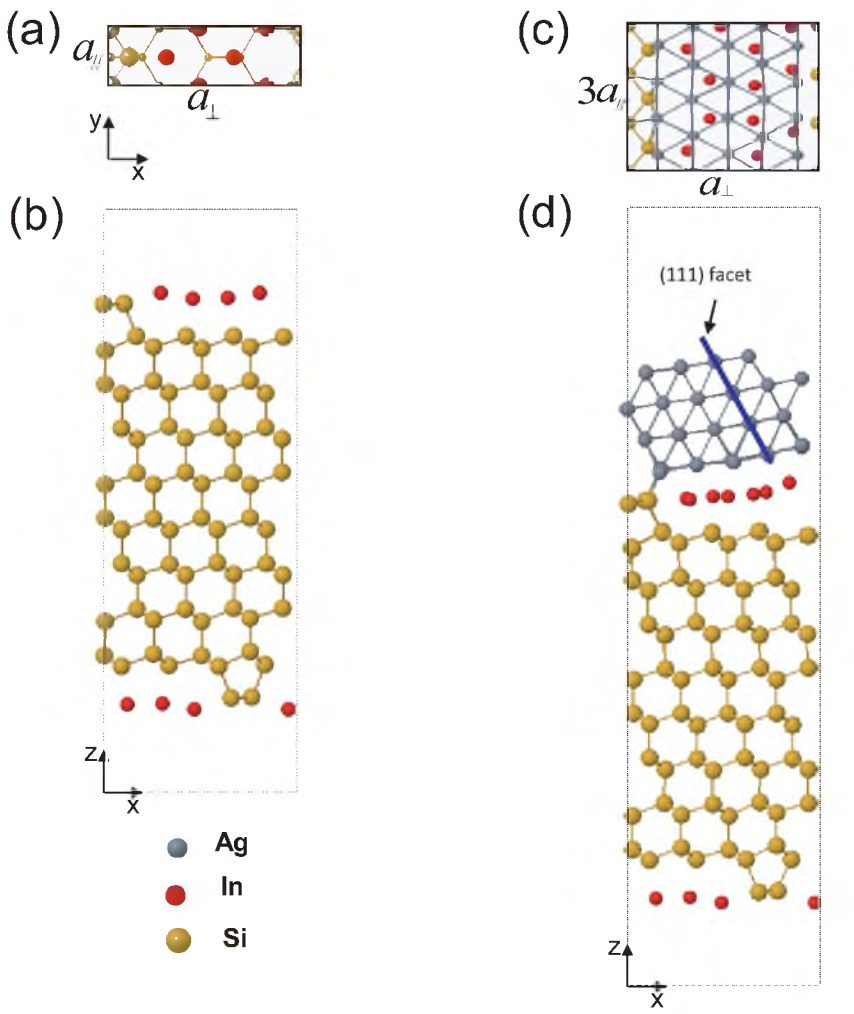

Figure 6.3. The atomic structure of supercell for calculation (a) Top view of 4×1 In/Si(111) reconstruction surface; (b) Side view of the supercell, having symmetry In/Si structure on both top and bottom sides; (c) Interface between Ag and In/Si surface after geometry optimization; (d) Side view of (b) with Ag layers on top side after geometry optimization.

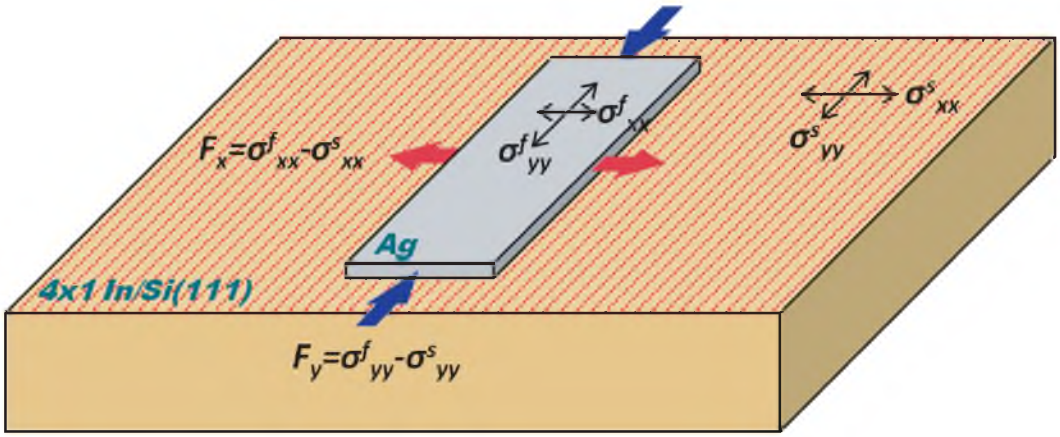

Figure 6.4. Schematic diagram of the stress of the system. The stress of the 4×1 In/Si (111) substrate template is σ^s. σ^f stand for the stress of the Ag/In/Si surface structure, and $F = \sigma^f - \sigma^s$ is the net stress on the 4-layer silver film.

ZG models [2,6,14]. There are three fitting parameters: $\alpha = \frac{\sqrt{E_x E_y}}{E_s}$, the ratio of island boundary energy and strain energy, where E_x (E_y) is the island boundary energy along the x-axis (y-axis) and $E_s = CF_x^2$ is the unit strain energy due to interaction between two force monopoles and C is the combination of elastic constants [6]; $\beta = \frac{\sqrt{E_y}}{\sqrt{E_x}}$, the ratio of island boundary energy in the two directions; and $\gamma = \frac{F_y}{F_x}$, the ratio of force monopole along y- and x-axis. It is impossible to determine quantitatively all these parameters, which also vary with temperature and island size. To simplify the fitting, we consider the following general trends of change in α, β and γ:(1) $\alpha \sim 1.0$ at LT, assuming the average boundary energy and unit strain energy is of the same order of magnitude; it decreases to a smaller value at RT because boundary energy decreases with increasing temperature (entropic effect) while strain energy is less sensitive to temperature. (2) β increases with the increasing temperature because island boundary energy becomes more isotropic at higher temperature. (3) $\gamma = -0.725$ at LT as obtained from the first-principles calculations at zero temperature; it changes with temperature [3] and falls into the range of $-1.5 < \gamma < -0.95$ at RT for the occurrence of the bistability. (4) Both α and β increase with the increasing island width (n), assuming the island boundary energy, E_y increases with the increasing island width while E_x remains constant because the wider Ag island covering more In chains (atomic rows) allows less y-edge relaxation in the direction perpendicular to the In chain, while the relaxation at the x-edge is insensitive to island width.

Based on the above considerations, we first fit the island base aspect ratio as a function of island size at LT, as shown in Fig. 6.2(a) for each branch of data of different island widths with $\gamma = -0.725$ and (1) $n = 2 :\ \alpha = 0.50$, $\beta = 0.31$; (2) $n = 3 :\ \alpha = 0.85$, $\beta = 0.65$; (3) $n = 4 :\ \alpha = 1.00$, $\beta = 0.85$; Next, using smaller α and β, we fit the experimental data at RT [Fig. 6.2(b)] for three branches of island widths with $\gamma = -1.05$ and (1) $n = 2 :\ \alpha = 0.10$, $\beta = 0.35$; (2) $n = 3 :\ \alpha = 0.50$, $\beta = 0.74$. The very good agreement between the theoretical fit and the experiment data indicate that the theoretical model is likely to be qualitatively correct, providing a feasible explanation for the experimentally observed bistability.

We have used a 2D model that correctly predicts the existence of the "bistability" and reveals its most salient features. This is because the Ag islands have

predominantly a flat top geometry and fixed height (4 ML), especially before the critical bifurcation point. However, the model prediction is not accurate for the compact island evolution beyond the critical point in Fig. 6.2(b). If the model is exactly followed, the compact islands should in principle grow both length and width simultaneously in order to keep the isotropic shape beyond the critical point. This, however, is somewhat prohibited because the width cannot grow continuously except by jumping in the multiples of In chain width on the template surface. Consequently, some compact islands grow in height into 3D islands and have an aspect ratio slightly larger than one [see Fig. 6.2(b)].

6.4 Conclusion

In conclusion, we have observed an intriguing growth phenomena in Ag deposition on Si(111)-(4×1)-In template surface, where compact isotropic Ag nanodots coexist with elongated anisotropic nanowires at RT. We believe the observed dual island shapes, in contrast to the conventional behavior of singular stable island shape at LT, provides a direct experimental evidence for the bistability of "anisotropically" stressed islands as recently predicted by Zandvliet and van Gastel [14]. Our first-principles calculations confirms that the Ag islands on the Si(111)-(4×1)-In surface are indeed stressed in a manner that force monopoles at neighboring island boundaries point to the opposite directions, satisfying the mandatory condition required for the ZG model. Fitting the experimental data with the theoretical model shows the general trends of changes in island boundary energy with changing temperature and island size. We expect such bistability to occur more generally in other systems, and can be exploited for controlling growth of nanostructures on surface.

6.5 References

[1] J. Tersoff and R. M. Tromp, Phys. Rev. Lett. **70**, 2782 (1993).

[2] A. Li, F. Liu, and M. G. Lagally, Phys. Rev. Lett. **85**, 1922 (2000).

[3] V. Zielasek *et al.*, Phys. Rev. B **64**, 201320(R) (2001).

[4] R. van Gastel, N.C. Bartelt, and G.L. Kellogg, Phys. Rev. Lett. **96**, 036106 (2006).

[5] N.V. Medhekar, V.B. Shenoy, J.B. Hannon and R.M. Tromp, Phys. Rev. Lett. **99**, 156102 (2007).

[6] F. Liu, "Modeling and Simulation of Strain-Mediated Nanostructure Formation on Surface", in Handbook of Theoretical and Computational Nanotechnology, eds. M. Rieth and W. Schommers, Chapter 10, 577-625 (2006).

[7]A. Li *et al.*, Phys. Rev. Lett. **85**, 5380 (2000).

[8] A. Pradhan, N.Y. Ma and F. Liu, Phys. Rev. B **70**, 193405 (2004).

[9] J. Zang, A. Treibergs, Y. Han, and F. Liu, Phys. Rev. Lett. **92**, 105501 (2004).

[10] M.T. Middel, H.J. Zandvliet, and B. Poelsema, Phys. Rev. Lett. **88**, 196105 (2002).

[11]G. J. Xu *et al.*, Phys. Rev. B **68**, 235318 (2003).

[12] M. Yata, Phys. Rev. B **74**, 165407 (2006).

[13] I. Goldfarb, L. Banks-Sills, and R. Eliasi, Phys. Rev. Lett. **97**, 206101 (2006).

[14] H. J. W. Zandvliet and R. van Gastel, Phys. Rev. Lett. **99**, 136103 (2007).

[15] J.-L. Li *et al.*, Phys. Rev. Lett. **88**, 066101 (2002).

[16] M. Hupalo and M. C. Tringides, Phys. Rev. B **73**, 041405(R) (2006).

[17] M. Yakes *et al.*, Appl. Phys. Lett. **90**, 163117 (2007).

[18] T. Uchihashi *et al.*, Phys. Rev. Lett. **96**, 136104 (2006).

[19] G. Kresse, and J. Joubert, Phys. Rev. B **59**, 1758 (1999).

[20] N. Nagamura *et al.*, Phys. Rev. Lett. **96**, 256801 (2006).

[21] G. H. Lu and F. Liu, Phys. Rev. Lett. **94**, 176103 (2005).

APPENDIX

PUBLICATIONS

1. Miao Liu, Feng Liu, "Thickness-dependent Adatom-Adatom Binding Energy on Pb(111): Quantum Size Effect on Critical Nucleus", *In preparation*

2. Miao Liu, Feng Liu, "Quantum Manifestation of Elastic Constants in Nanostructures", *Submitted to Phys. Rev. Lett.*, (arXiv:1209.0865)

3. Miao Liu, Yong Han, Lin Tang, Jin-Feng Jia, Qi-Kun Xue, Feng Liu, "Interplay between Quantum Size Effect and Strain Effect on Growth of Nanoscale Metal Thin Film", *Phys. Rev. B 86, 125427 (2012)*

4. Hao Hu, Miao Liu, Z. F. Wang, Junyi Zhu, Dangxin Wu, Hepeng Ding, Zheng Liu, and Feng Liu, "Quantum Electronic Stress: Density-Functional-Theory Formulation and Physical Manifestation", *Phys. Rev. Lett. 109, 055501 (2012)*

5. Ninghai Su, Miao Liu and Feng Liu, "Chemical versus thermal folding of graphene edges", *Nano Res. 4, 1242 (2011)*

6. Yaoyi Li, Miao Liu, Dayan Ma, Decai Yu, Xi Chen, Xu-Cun Ma, Qi-Kun Xue, Kewei Xu, Jin-Feng Jia, and Feng Liu, "Bistability of nanoscale Ag islands on a Si(111)-(4×1)-In surface induced by anisotropic stress", *Phys. Rev. Lett. 103, 076102 (2009)*

7. Bing Huang, Miao Liu, Ninghai Su, Jian Wu, Wenhui Duan, Bing-lin Gu, and Feng Liu, "Quantum Manifestations of Graphene Edge Stress and Edge Instability: A First-Principles Study", *Phys. Rev. Lett. 102, 166404 (2009)*

8. Decai Yu, Elizabeth M. Lupton, Miao Liu, Wei Liu and Feng Liu, "Collective magnetic behavior of graphene nanohole superlattices", *Nano Res. 1, 56 (2008)*